UCLouvain

epl

École polytechnique de Louvain

From crystallisation to polydispersity: a multi-scale analysis of dry dense granular flows

Author: **Perrine Moons**
Supervisors: **Jonathan Lambrechts, Vincent Legat**
Readers: **Evelyne Van Ruymbeke, Michel Henry, Simon Yans**
Academic year 2025–2026
Master [120] in Mechanical Engineering

Abstract

Dense granular flows are encountered in many natural and industrial processes, yet their rheology remains incompletely understood. Using the open-source *MigFlow* software, this thesis investigates the rheology of dry dense granular materials through two-dimensional plane Couette shear simulations under imposed confinement pressure.

Monodisperse assemblies were first simulated across a range of inertial numbers to characterise the $\mu(I)$ rheology. The expected trends were recovered : the effective friction coefficient μ increases and the packing fraction ϕ decreases with the inertial number I, but below a critical value $I_c \in [0.14, 0.28]$, the system undergoes crystallisation-induced jamming and locks into a stable hexagonal lattice, making the rest of the dense regime inaccessible.

Polydisperse assemblies (uniform radius distribution, $\lambda = d_{\max}/d_{\min}$ up to 9) were introduced to avoid crystallisation. Studied down to $I \approx 10^{-3}$, increasing polydispersity raises the effective friction coefficient, and lowers the equilibrium packing fraction. The constitutive parameters of the $\mu(I)$ law were identified for each polydispersity level, and their monotonic dependence on λ was quantified.

In short, this thesis showed that the $\mu(I)$-rheology model was recovered for polydisperse assemblies using the *Migflow* framework.

Acknowledgements

First, I would like to thank my supervisors, Jonathan Lambrechts and Vincent Legat, for their guidance and availability throughout this work. I am also grateful to the readers, Evelyne Van Ruymbeke, Michel Henry, and especially Simon Yans, for their time and feedback. Finally, I would like to thank my close friends and family for their constant encouragement and support throughout this journey.

Contents

Introduction

Granular materials are assemblies of discrete macroscopic particles. They are among the most processed substances on Earth, trailing only water in industrial importance [1]. Their behaviour is central to civil engineering (soil stability, concrete design), chemical engineering (granular catalysts), pharmaceutics (powder handling), and geophysical hazard assessment (landslides, avalanches, pyroclastic flows). From sand and gravel to powders and rockfalls, their behaviour underpins a remarkable range of natural and technological phenomena. However, despite their ubiquity, granular assemblies remain incompletely understood [1, 2, 3, 4, 5, 6]: depending on the applied stress or confinement, they can behave as rigid solids, yield abruptly, or flow like viscous fluids, often switching between these states in ways that are difficult to predict.

The rheology of granular media therefore remains an active area of research [7, 8, 9]. A central challenge in granular mechanics is the link between the microscopic particle interactions, such as contact forces, friction, geometry, and the macroscopic behaviour that governs large-scale flows. Addressing this multi-scale problem requires both theoretical frameworks and numerical tools capable of resolving grain-level dynamics [10] while extracting bulk rheological properties.

The objective of this thesis is to characterise the $\mu(I)$ rheological response [11] of dense dry granular media through two-dimensional plane Couette simulations. More specifically, the work aims to identify the conditions under which a dry monodisperse system undergoes crystallisation-induced jamming and to quantify the effect of polydispersity on the macroscopic rheology and microstructure.

The simulations are conducted using *MigFlow* [12], an open-source framework based on a Non-Smooth Contact Dynamics (NSCD) method, which handles the granular contact mechanics. Although *MigFlow* also supports coupled fluid-granular simulations, in this work only its dry granular solver is used. The configuration studied is a two-dimensional plane Couette flow under imposed confining pressure, which allows the packing fraction to evolve freely and provides direct access to the pressure-controlled rheological framework.

This thesis is organised as follows. Chapter 1 provides a state-of-the-art overview

of the rheology of granular media, from the historical foundations and theoretical frameworks to the constitutive law $\mu(I)$ and the concept of polydispersity. Chapter 2 describes the numerical methodology: the physical problem, the *MigFlow* framework, the implementation, and the post-processing procedure. Chapter 3 presents and analyses the simulation results for mono- and polydisperse assemblies.

Chapter 1

Rheology of granular media

Granular media constitute a fascinating and ubiquitous category of materials and despite the large morphological and material diversity of their individual components, they are governed by universal physical principles [1]. At the microscopic scale, granular materials are disordered assemblies of discrete macroscopic particles. Yet, they display complex emergent macroscopic behaviours, including arch formation, size segregation, and avalanche dynamics [4], which contrasts with the traditional distinction between solid- and fluid-like states.

The objective of this chapter is twofold. It first provides a state-of-the-art overview of the physics and rheology of granular materials: fundamental properties of granular media, historical foundations of rheology, and the theoretical framework of the inertial number and $\mu(I)$ rheological law. It then reviews the main numerical approaches used to simulate such systems, from continuum frictional models to multiphase formulations, and motivates the discrete-element approach adopted in this work.

1.1 Classification of particulate systems

The term particulate matter covers a broad spectrum of discrete-particle systems, which are commonly classified according to their characteristic particle size d [1], as illustrated in figure 1.1. At the smallest scales, colloids ($d < 1\,\mu$m) are dominated by Brownian motion, which continuously randomises particle configurations and renders equilibrium statistical mechanics applicable [13]. In the intermediate powder regime ($1\,\mu\text{m} < d < 100\,\mu\text{m}$), surface-to-volume ratios increase significantly and forces such as van der Waals attraction, electrostatic interactions, and interstitial fluid drag begin to compete with direct contact forces. Beyond $100\,\mu$m lies the granular regime, which is the focus of this work.

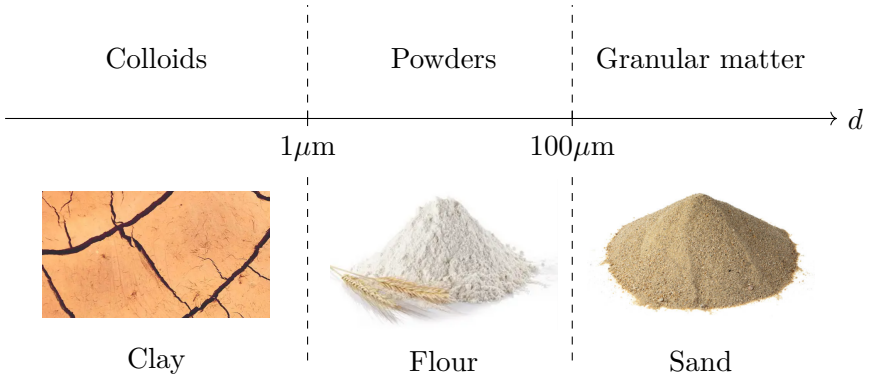

Figure 1.1: Classification of particulate matter by characteristic particle size d: colloids ($d < 1\,\mu m$), powders ($1\,\mu m < d < 100\,\mu m$), and granular matter ($d > 100\,\mu m$), illustrated by representative examples (clay [1], flour [2], and sand [3], respectively).

In the granular regime, the system is strictly athermal [4]: the kinetic energy carried by ambient thermal fluctuations is negligibly small compared to the gravitational potential energy of a single grain, so that thermal agitation plays no role whatsoever in the macroscopic dynamics. Granular materials are furthermore inherently dissipative, as energy is irreversibly lost through static friction and inelastic collisions at inter-particle contacts. Their dynamics is governed almost exclusively by the evolution of the internal contact network [2] and unlike colloidal suspensions, granular assemblies can remain trapped in metastable configurations indefinitely.

A particularly striking manifestation of this is jamming [14, 15, 16]: the abrupt transition from a flowing to a solid-like state when the packing fraction or applied stress exceeds a critical threshold [14], at which point a system-spanning network of force chains [2, 17] prevents any particle rearrangements. Below this threshold, the assembly flows freely; above it, the contact network becomes mechanically rigid and the material behaves as a disordered solid.

[1] https://www.bioandco.bio/largile-remede-vieux-monde/
[2] https://cuisine-facile.com/les-farines.php
[3] https://www.istockphoto.com/fr/photo/pile-de-sable-gm157506893-10960361

1.2 Historical foundations of rheology

Rheology, derived from the Ancient Greek words ῥέω ("to flow") and λόγος ("study"), is the science of deformation and flow of matter under applied stress [18]. Formally established as a discipline in 1929 with the founding of the American Society of Rheology, it has since become central to the understanding of a wide range of natural and industrial materials: concrete, polymer melts, food pastes, inks, and volcanic lava, among many others.

The two cornerstones of rheology are the idealised models of Robert Hooke and Isaac Newton, which describe the limiting behaviours of purely elastic solids and purely viscous fluids, respectively. In his *De Potentia Restitutiva* (1678) [19], Hooke established that, within small deformations, the stress σ developed in a solid is proportional to the applied strain ε:

$$\sigma = E\,\varepsilon$$

where E is the Young's modulus. A Hookean solid stores deformation energy elastically and returns to its original shape upon removal of the load, as illustrated in figure 1.2.

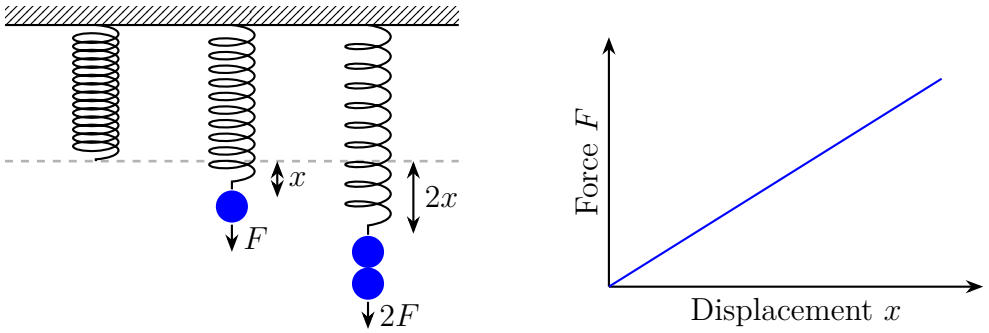

Figure 1.2: Illustration of Hooke's law: doubling the applied force doubles the displacement, reflecting the linear stress–strain relationship.

Newton, in his *Principia Mathematica* (1687) [20], proposed an analogous linearity for fluids, as illustrated in figure 1.3. The shear stress τ required to maintain flow is proportional to the velocity gradient between adjacent fluid layers, i.e. to the shear rate $\dot{\gamma}$:

$$\tau = \eta\,\dot{\gamma}$$

where η is the dynamic viscosity. A Newtonian fluid dissipates energy entirely through viscous friction and exhibits no elastic recovery.

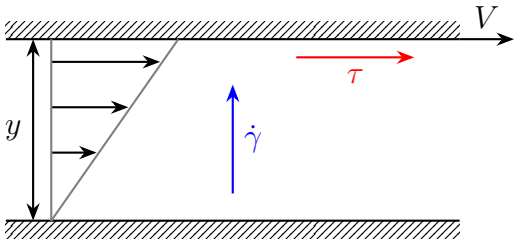

Figure 1.3: Illustration of Newton's law of viscosity: a linear velocity profile develops between a fixed lower wall and a moving upper wall, generating a uniform shear rate $\dot{\gamma}$ and a shear stress τ.

These two idealised models represent opposite extremes of material behaviour. Most real substances fall somewhere between them [18], exhibiting a combination of viscous and elastic responses known as viscoelastic behaviour, well documented within the framework of polymers in Ferry's work [21]. Such materials deform gradually under sustained stress, recover only partially upon unloading, and display complex time-dependent responses that neither Hooke's nor Newton's law can capture alone.

Granular media occupy a particularly singular position in this landscape. Depending on the applied stress and packing conditions, they can behave as a rigid solid, flow like a viscous fluid, or transition abruptly between these states. This dual nature makes them simultaneously challenging and fascinating from a rheological standpoint, and motivates the theoretical framework developed in the following sections.

1.3 Inertial number and rheological laws for dry granular flows

In order to characterise the competition between external driving and internal relaxation of dry granular flows, an important dimensionless parameter is introduced. Because dry granular media rely solely on contact forces and particle inertia, the appropriate dimensionless number is the inertial number:

$$I = \frac{\dot{\gamma}\, d}{\sqrt{P^p/\rho_p}}, \tag{1.1}$$

with d denoting the characteristic length scale of the particle (usually its diameter), ρ_p the particle density, $\dot{\gamma}$ the shear rate, and P^p the confining pressure.

This inertial number I provides a dimensionless characterisation of the flow [8, 9] by comparing two distinct time scales: the macroscopic deformation time imposed by the shear rate, $\tau_\gamma = 1/\dot{\gamma}$, and the microscopic rearrangement time required for a particle to move by one diameter under the confining pressure, $\tau_c = d/\sqrt{P^p/\rho_p}$. Physically, I measures the competition between external shearing and the statistical relaxation of the granular microstructure.

Depending on the value of I, three distinct flow regimes can be identified [22], as shown in figure 1.4:

- Quasi-static regime ($I \leq 10^{-3}$): Deformation is very slow compared to the time needed for particle rearrangement. The material behaves like a solid close to yielding, with grains forming a persistent force network that carries stress. This corresponds physically to slowly deforming soils, silo discharge at very low rates, or the creeping motion of a pile.
- Dense inertial regime ($10^{-3} \leq I \leq 1$): The timescales of deformation and rearrangement become comparable. Contacts between grains are frequent but short-lived, and collisions start to contribute. This regime governs dense granular flows such as grains flowing down inclined planes, dense avalanches, or industrial mixers.
- Collisional (kinetic) regime ($I \geq 1$): The shear rate is so large that particles cannot form lasting contacts. Interactions are dominated by instantaneous binary collisions, and the material behaves analogously to a molecular gas. Kinetic theory becomes relevant.

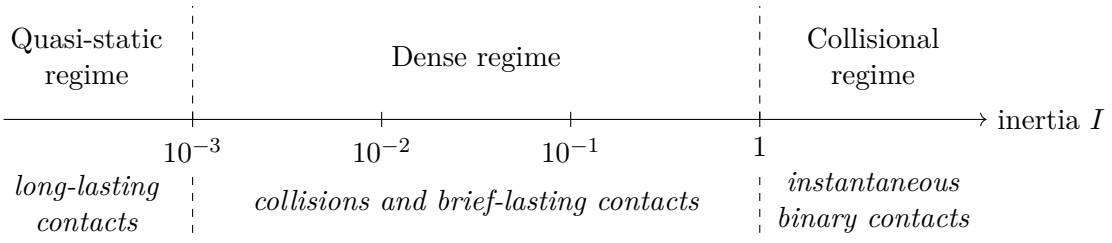

Figure 1.4: Flow regimes of dry granular media as a function of the inertial number I: quasi-static regime ($I \leq 10^{-3}$, long-lasting contacts), dense inertial regime ($10^{-3} \leq I \leq 10^{-1}$, short-lived contacts and collisions), and collisional regime ($I \geq 10^{-1}$, instantaneous binary contacts).

In the dry case, the constitutive laws relating the macroscopic stress state to the flow kinematics take the form:

$$\tau = \mu(I)\, P^p, \qquad \phi = \phi(I),$$

where $\mu(I)$ is an effective friction coefficient and $\phi(I)$ is the solid volume fraction. Among the different approaches proposed [8, 9, 11, 22], the $\mu(I)$ rheology has emerged as a simple and powerful model to describe dense granular flows. It relates the effective friction coefficient to the inertial number and describes a continuous transition between the quasi-static and the strongly inertial regime.

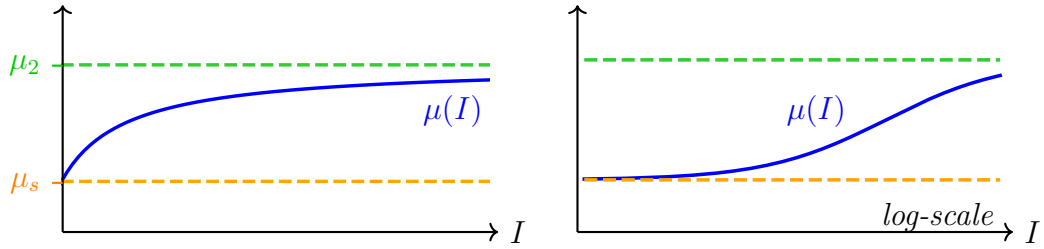

Figure 1.5: Effective friction coefficient μ as a function of the inertial number I (left: linear scale, right: logarithmic scale), as described by the $\mu(I)$-law (equation 1.2). The coefficient increases monotonically from the quasi-static threshold μ_s toward the inertial limit μ_2, with I_0 setting the scale of the transition.

In the limit $I \to 0$, the granular material behaves as a solid with a critical friction coefficient μ_s, corresponding to the threshold for flow initiation. As I increases, friction gradually increases and converges towards a limiting value μ_2, associated with rapid shear conditions. This evolution is captured by the empirical law [11, 23]:

$$\mu(I) = \mu_s + \frac{\mu_2 - \mu_s}{I_0/I + 1}, \tag{1.2}$$

where I_0 is a material-dependent constant that sets the characteristic scale of the transition between the two regimes. This formulation has successfully reproduced several granular flow configurations, including velocity profiles on inclined planes and key features of heap flows. However, this scalar law remains limited, as it cannot describe more complex flows where multiple shear directions interact, requiring a full three-dimensional rheological framework.

1.3.1 Polydispersity

While the $\mu(I)$ rheology introduced above provides a robust description of dense granular flows, it was derived under the assumption of monodisperse assemblies, where all particles share the same diameter. In real-world granular systems, however, particles are rarely identical in size. They exhibit a distribution of grain dimensions known as polydispersity, illustrated in figure 1.6. Understanding how this size distribution affects the rheological response is therefore essential before extending the framework to more realistic configurations.

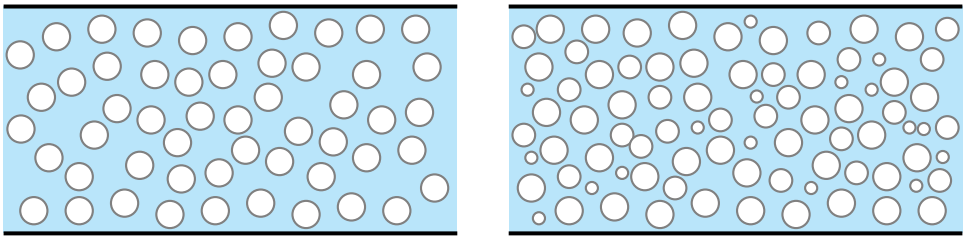

Figure 1.6: Schematic illustration of monodisperse (left) and polydisperse (right) particle assemblies, highlighting the contrast between a uniform grain size and a broad size distribution.

Quantification of polydispersity

Polydispersity is characterised by the grain size distribution $f(d)$, representing the probability density of finding a particle of diameter d. To quantify the width of this distribution, the polydispersity index can be used:

$$PDI = \frac{\sigma_d}{\langle d \rangle},$$

where σ_d is the standard deviation and $\langle d \rangle$ is the mean diameter. A low PDI indicates a relatively uniform assembly, whereas a high PDI signifies a broad range of particle sizes.

Another widely used metric is the polydispersity level [9], defined as

$$\lambda = d_{max}/d_{min},$$

where d_{max} and d_{min} denote the maximum and minimum grain diameters in the sample.

Characteristic length scale in polydisperse systems

A central difficulty in extending the inertial number (eq. 1.1) to polydisperse systems lies in the choice of a characteristic length scale. While monodisperse systems naturally use the particle diameter d, polydisperse systems face the problem of a varying diameter due to the size distribution.

Several alternatives exist in heterogeneous assemblies. A naive choice such as the arithmetic mean diameter may fail to capture mechanical interactions, since contact mechanics are controlled by local geometry rather than global averages. Similarly, extreme values such as d_{max} or d_{min} are not representative of the bulk behaviour, as they respectively overestimate or underestimate the effective interaction scale.

A recent study by Polanía [9] suggests that a more relevant quantity is the average

branch length, defined as the mean centre-to-centre distance between contacting particles:

$$\ell_b = \langle |\mathbf{r}_i - \mathbf{r}_j| \rangle_{\text{contacts}}.$$

This quantity emerges naturally from the contact network and reflects the actual geometric scale of force transmission, as illustrated in figure 1.7. It therefore constitutes the most physically grounded choice for the characteristic length scale entering the inertial number in polydisperse systems, and will be adopted throughout this work.

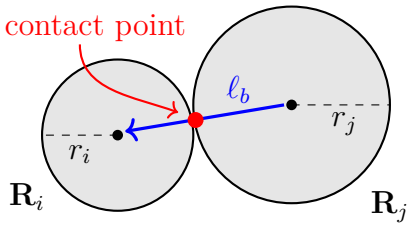

Figure 1.7: Illustration of the branch length ℓ_b, defined as the centre-to-centre distance between two contacting particles.

1.4 Numerical approaches for granular flows

The physical framework established in the previous sections (effective friction, the inertial number, and constitutive laws) must be translated into numerical models to simulate granular flows in complex geometries. Two broad families of approaches exist: continuum methods, which treat the granular assembly as an effective medium, and multiphase methods, which resolve the coupling between a discrete solid phase and a continuous fluid phase. This section reviews both families, with particular attention to their underlying assumptions and their domains of applicability.

1.4.1 Continuum approaches: frictional rheology

Frictional rheology provides a family of continuum constitutive laws that express the macroscopic stress state of a granular or suspended system as a function of a single dimensionless flow parameter. Depending on whether an interstitial fluid is present or absent, this parameter is either the viscous number J or the inertial number I introduced in section 1.3. In both cases, the resulting constitutive law can be embedded directly in a finite-element method (FEM) solver, where the material is treated as a single effective fluid with a non-linear, state-dependent viscosity.

Dry granular flows: the $\mu(I)$ law in a FEM solver

The $\mu(I)$ rheology presented in section 1.3 provides a local, scalar constitutive law that directly connects the stress state to the kinematics of the flow. This compactness makes it particularly well suited for implementation within a continuum solver, where the granular assembly is treated as a single effective fluid whose viscosity depends on the local flow conditions.

In this continuum description, the granular medium is governed by the incompressible Navier-Stokes equations with a pressure- and shear-rate-dependent effective viscosity η_{eff}. From the constitutive relation $\tau = \mu(I)\, P^p$ and the definition of the inertial number, one can derive:

$$\eta_{\text{eff}}(\dot{\gamma}, P^p) = \frac{\mu(I)\, P^p}{\dot{\gamma}} = \mu\left(\frac{\dot{\gamma}\, d}{\sqrt{P^p/\rho_p}}\right) \frac{P^p}{\dot{\gamma}},$$

which defines a non-Newtonian viscosity that diverges as $\dot{\gamma} \to 0$ (quasi-static limit) and decreases as $\dot{\gamma}$ increases (shear-thinning behaviour). This formulation can be embedded straightforwardly in a FEM solver [11]: the granular momentum equations are discretised over the domain, and the non-linear effective viscosity is updated iteratively at each integration point from the local pressure and shear rate.

This approach has been successfully used to simulate dense granular flows on inclined planes, in hoppers, and around obstacles, capturing mean velocity profiles and free-surface shapes with good accuracy [11, 23]. Its main advantages are computational efficiency and the direct use of well-established FEM infrastructure.

However, the continuum $\mu(I)$ approach has intrinsic limitations. Being a local scalar law, it cannot capture non-local effects such as creep in nearly arrested regions, where distant flowing zones can mobilise grains far below the yield threshold [23]. It also assumes a perfectly dense, monodisperse material, and provides no information on individual particle trajectories, force distributions, or structural rearrangements.

Dense suspensions: the viscous number J and frictional rheology

When an interstitial fluid is present, the natural continuum analogue of the $\mu(I)$ law is the frictional rheology based on the viscous number J. Rather than tracking the detailed fluid-particle interaction forces through a full two-phase formulation, one seeks directly a constitutive law relating the macroscopic stresses to the kinematic state of the suspension. The relative importance of viscous and particle stresses is captured by the single dimensionless parameter

$$J = \frac{\eta_f \dot{\gamma}}{P^p},$$

representing the ratio of a typical viscous stress $\eta_f \dot{\gamma}$ to the particle pressure P^p. Typical values in dense suspension flows are $J \sim 10^{-4} - 10^{-1}$. For small J, particle pressure dominates and the suspension exhibits granular-like behaviour; for large J, viscous stresses dominate and the suspension approaches Newtonian behaviour.

Constitutive laws can then be expressed compactly as

$$\tau = \mu(J)\, P^p, \qquad \phi = \phi(J),$$

where $\mu(J)$ is an effective friction coefficient and $\phi(J)$ the volume fraction corresponding to a given viscous number. This formulation provides a complete closure: the macroscopic response is described by two scalar functions of J, and can be implemented in a FEM solver in a manner directly analogous to the $\mu(I)$ law [24].

The frictional approach also bridges two complementary experimental descriptions of suspensions, illustrated in figure 1.8. In volume-imposed rheology, the volume fraction ϕ is fixed and the shear stress and particle pressure are measured:

$$\tau = \eta_s(\phi)\, \eta_f \dot{\gamma}, \qquad P^p = \eta_{n,2}(\phi)\, \eta_f \dot{\gamma}.$$

In pressure-imposed rheology, the particle pressure P^p is fixed and the system responds through its shear stress and volume fraction:

$$\tau = \mu(J)\, P^p, \qquad \phi = \phi(J).$$

For steady simple shear, these two descriptions are equivalent, with the relationships

$$\eta_{n,2}(\phi) = \frac{1}{J(\phi)}, \qquad \eta_s(\phi) = \frac{\mu(\phi)}{J(\phi)},$$

where $J(\phi)$ is the inverse function of $\phi(J)$. Pressure-imposed rheology facilitates the study of flows near jamming by allowing ϕ to fluctuate, avoiding the transient divergence of the viscosities.

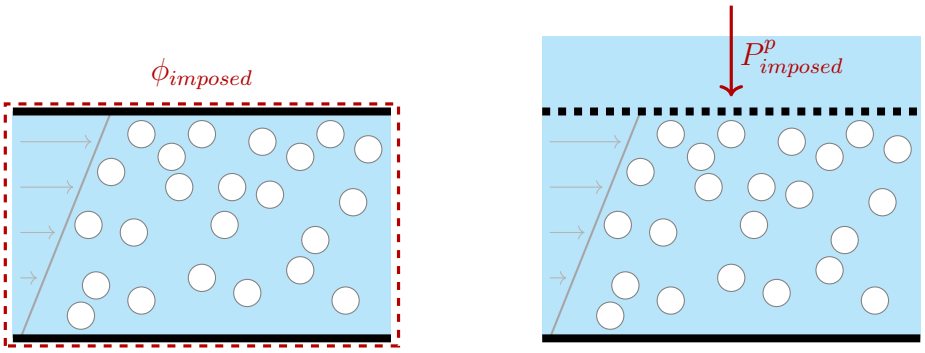

Figure 1.8: Schematic comparison of the two complementary rheological approaches for dense suspensions: volume-imposed rheology (fixed ϕ, measured τ and P^p) and pressure-imposed rheology (fixed P^p, measured τ and ϕ).

The limitations of this continuum frictional approach for suspensions mirror those of the $\mu(I)$ law: it is a scalar, local closure that cannot resolve particle-scale heterogeneities, phase separation, or structural rearrangements. When these phenomena are important, a more detailed multiphase description is required.

1.4.2 Multiphase approach

When the relative motion between the solid and fluid phases cannot be neglected, a single effective-fluid description is insufficient. The multiphase approach treats the solid and fluid phases as distinct interacting continua, providing a richer description of the coupled dynamics [24].

In the single-phase description, the relative motion between the solid particles and the surrounding fluid is entirely neglected. However, this assumption breaks down whenever spatial gradients of the flow give rise to net forces acting differently on the two phases. In such cases, a two-phase description becomes necessary, in which the liquid and solid phases are treated separately, with mass and momentum conservation equations applied individually to each phase.

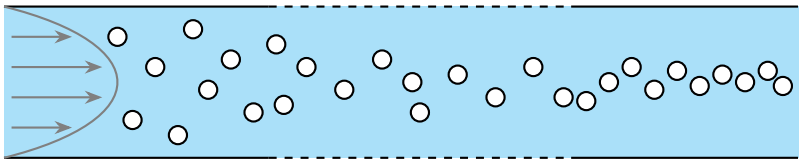

Figure 1.9: Shear-induced migration of neutrally buoyant spheres in a pressure-driven Poiseuille flow: particles migrate from the high-shear regions near the walls toward the low-shear centreline.

This approach is particularly relevant for phenomena such as erosion, avalanches, or shear-induced particle migration (figure 1.9). The driving mechanism is the gradient of particle pressure: particles are pushed away from regions where the particle pressure, and thus also the shaer rate, is highest [24].

A key quantity in this description is the particle pressure P^p, which quantifies the internal stresses carried by the particle phase. While the suspension as a whole is incompressible, collisions between particles and interactions with the walls can still create pressure within the particle phase. This positive particle pressure is therefore balanced by a corresponding negative pressure in the fluid phase, maintaining the overall incompressibility of the mixture, as illustrated in figure 1.10.

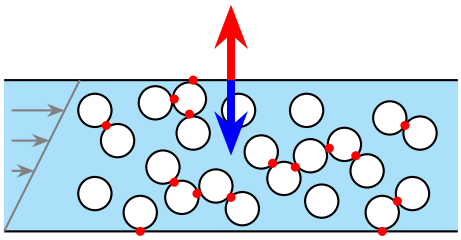

Figure 1.10: Sheared suspension between two walls. Particle contacts (red dots) give rise to a particle pressure P^p acting normal to the wall (red arrow), while the fluid phase develops an equal and opposite pressure response (blue arrow) to maintain overall incompressibility.

Particle normal stresses scale viscously and are typically linear with the applied shear rate:

$$-\sigma_{22}^P = \eta_{n,2}\,\eta_f|\dot{\gamma}|,$$

where $\eta_{n,2}$ is the relative normal viscosity. The ratio of particle normal stress to shear stress defines the macroscopic effective friction coefficient of the suspension:

$$-\frac{\sigma_{22}^P}{\tau} = \frac{\eta_{n,2}}{\eta_s} = \frac{1}{\mu}.$$

1.4.3 Governing equations

From a modelling perspective, the exact calculation of particle motion in a Newtonian fluid requires solving Newton's equations for each particle coupled with the Navier-Stokes equations for the fluid with boundary conditions on each particle surface. Although this description is physically exact, it rapidly becomes impractical: tracking every particle and solving the fluid flow around each individually is computationally prohibitive even for moderately sized systems.

To overcome this difficulty, continuum two-phase modelling is commonly adopted and the fluid and particle phases are treated as two intertwined continuous media. In practice, this simply means that the observation scale is changed. Rather than describing every particle position, a small region of space around a point $\mathbf{x}$ is considered. This region is large enough to contain many particles but remains small compared to the macroscopic scale of the system. This requirement introduces a separation of scales

$$d_p \ll r_0 \ll L$$

where d_p is the particle diameter, r_0 is the size of the averaging region, and L is the characteristic macroscopic length scale of the system, as illustrated in figure 1.11. This condition ensures that the averaging region contains a statistically

representative number of particles while still resolving the spatial variations of the flow.

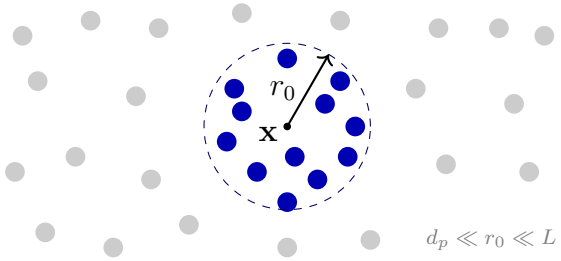

Figure 1.11: Illustration of the spatial averaging over a representative domain of radius r_0 centred on a point $\mathbf{x}$, with $d_p \ll r_0 \ll L$ ensuring scale separation between the particle diameter d_p and the macroscopic length scale L.

Governing equations can then be derived in an averaged sense for each phase, capturing the essential dynamics of the suspension without explicitly resolving individual particle motions. Multiple attempts have been made in the literature to simplify the problem using this method, as done by Anderson and Jackson [25, 26].

Their approach consists of replacing point-wise mechanical variables with local mean quantities, obtained by spatially averaging. To do so, a weighting function $g(r)$, illustrated in figure 1.12, is introduced to assign distance-dependent weights to neighbouring points around $\mathbf{x}$: nearby points contribute more strongly to the average than distant ones. The function is positive, smooth, and normalised to unity, while its characteristic radius r_0 defines the effective size of the averaging region.

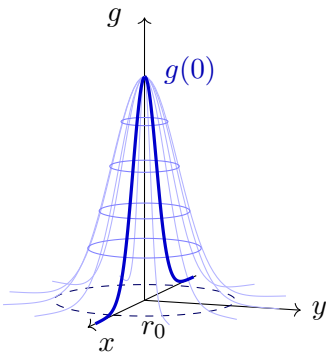

Figure 1.12: Weighting function g(r) used in the spatial averaging procedure of Anderson and Jackson.

Another powerful mathematical tool used by Anderson and Jackson is a decomposition similar to the Reynolds decomposition used in turbulence modelling. Any

point variable $u'(\mathbf{x}, t)$ can be decomposed into its slowly varying local mean value $u(\mathbf{x}, t)$ and a sub-filter fluctuation $u''(\mathbf{x}, t)$ of zero-mean:

$$u'(\mathbf{x}, t) = u(\mathbf{x}, t) + u''(\mathbf{x}, t)$$

as illustrated in figure 1.13. This decomposition is the cornerstone of the averaging procedure: it allows the governing equations to be written in terms of smooth, slowly varying mean fields, while the effect of sub-scale fluctuations is captured through additional closure terms.

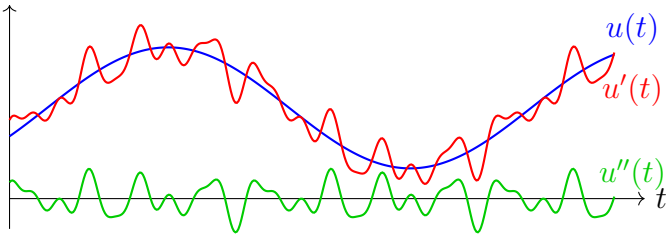

Figure 1.13: Reynolds decomposition of a signal $u'(\mathbf{x}, t)$ (red) into a local mean $u(\mathbf{x}, t)$ (blue) and a sub-filter fluctuation $u''(\mathbf{x}, t)$ (green).

Using this framework, averaged quantities describing each phase are defined inside the averaging domain. The most important one is the local void fraction $\varepsilon(\mathbf{x}, t)$, which represents the fraction of the local volume occupied by the fluid. The complementary fraction $1 - \varepsilon(\mathbf{x}, t)$ corresponds to the particles. Mean velocities of both phases are also defined: the fluid velocity $\mathbf{u}(\mathbf{x}, t)$ and the particle velocity: $\mathbf{v}(\mathbf{x}, t)$. Rather than describing each particle individually, the model describes the system statistically: in a given region, a fraction $1 - \varepsilon$ of the volume is occupied by particles moving with average velocity $\mathbf{v}$.

According to Anderson and Jackson [26], the mass conservation equations for the fluid and the particles are:

$$\frac{\partial \varepsilon}{\partial t} + \nabla \cdot (\varepsilon \mathbf{u}) = 0$$

$$\frac{\partial (1-\varepsilon)}{\partial t} + \nabla \cdot ((1-\varepsilon)\mathbf{v}) = 0$$

These equations are very similar to the classical continuity equation of fluid mechanics. The main difference is that each term is multiplied by the corresponding volume fraction.

Starting from the Navier-Stokes equations for the fluid and applying the spatial averaging procedure leads to a momentum equation for the fluid phase of the form:

$$\rho_f \varepsilon \left(\frac{\partial \mathbf{u}}{\partial t} + \mathbf{u} \cdot \nabla \mathbf{u} \right) = \nabla \cdot \mathcal{E} - n\mathbf{f}^{fp} + \varepsilon \rho_f \mathbf{g}.$$

with n the local mean particle density. Similarly, the particle phase satisfies:

$$\rho_s(1-\varepsilon)\left(\frac{\partial \mathbf{v}}{\partial t}+\mathbf{v}\cdot\nabla\mathbf{v}\right)=n\mathbf{f}^{fp}+n\mathbf{f}^{pp}-\nabla\cdot S^s+(1-\varepsilon)\rho_s\mathbf{g}.$$

These equations resemble the classical momentum equation of fluid mechanics, but they include additional terms representing the interaction between phases. In particular:

- $\mathbf{f}^{fp}$ represents the force exerted by the surrounding fluid on each particle,
- $\mathbf{f}^{pp}$ represents the force exerted on each particle as a result of direct contact with other particles
- S^s represents stresses arising from particle interactions,
- $\mathcal{E}$ contains the effective fluid stresses.

The equations above describe the conservation of mass and momentum for each phase. However, this gain in tractability comes at a cost. By averaging out the microscopic degrees of freedom, the procedure introduces new unknown terms (the interaction force $\mathbf{f}$, the particle stress S^s, and the effective fluid stress $\mathcal{E}$) which cannot be determined from the averaged equations alone. Additional models are therefore required to express these terms as functions of the resolved quantities: the void fraction, the phase velocities, the pressure, and the fluid properties. Providing these relations constitutes the closure problem of two-phase flow modelling.

1.4.4 MigFlow: a coupled FEM–DEM framework

MigFlow [12] is an unresolved CFD-DEM framework designed for immersed granular flows. Rather than resolving the fluid flow at the scale of individual particles, it couples a finite-element solver for the fluid phase with a discrete-element method for the solid phase, operating at two distinct scales.

The fluid phase is governed by the averaged Navier–Stokes equations discretised on a coarse finite-element mesh. The solid phase is handled by a DEM solver [10], in which each particle is tracked individually through Newton's equations of motion, accounting for contact forces with neighbouring particles and boundaries. The coupling between the two phases is realised through an empirical drag law that parametrises the momentum transfer: the local void fraction ε, computed from the particle positions, enters directly into the fluid momentum equation, while the resulting fluid-particle interaction force $\mathbf{f}^{fp}$ is applied back to each particle.

This unresolved approach offers a favourable compromise between the computational efficiency of continuum methods and the particle-scale resolution of fully discrete approaches.

1.4.5 Summary and choice of numerical approach

The numerical approaches reviewed above span a wide spectrum of complexity and applicability. The continuum $\mu(I)$ and $\mu(J)$ approaches offer computational efficiency within a FEM framework, but rely on local constitutive assumptions and cannot resolve particle-scale physics. Two-phase formulations provide a more rigorous description of both phases and MigFlow couples a FEM fluid solver with a DEM solid solver, resolving particle dynamics individually while describing the fluid through averaged equations.

The present work focuses on dry dense granular flows, where the interstitial fluid is absent and the governing physics reduces entirely to the regime characterised by the inertial number I. The DEM alone is therefore the natural choice: by tracking each particle individually, it provides direct access to inter-particle forces, contact network topology, and particle-scale kinematics without any averaging assumption. Macroscopic quantities such as $\mu(I)$ can then be recovered a posteriori rather than imposed, making DEM an ideal tool for investigating the microscopic origins of macroscopic granular behaviour and extending rheological models to polydisperse assemblies.

Chapter 2

Methodology

The previous chapter introduced the theoretical and numerical frameworks used to describe the rheology of dense granular media, and motivated the use of the Discrete Element Method (DEM) as the simulation tool of choice for dry granular flows. In this context, the DEM provides direct access to inter-particle forces, contact network topology, and particle-scale kinematics. These quantities are inaccessible to continuum approaches but essential for understanding the microscopic origins of macroscopic rheological behaviour.

The objective of this chapter is to present the numerical methodology adopted to investigate the rheology of dense dry granular systems subjected to simple shear. The simulations are performed using the open-source framework *MigFlow*, whose granular component implements an implicit DEM with non-smooth contact dynamics (NSCD).

The chapter is organised as follows. The physical problem and the modelling assumptions are first introduced. The DEM framework is then presented in detail. The implementation of this framework within *MigFlow* is subsequently described, including boundary conditions and the periodic remapping procedure. Finally, the post-processing methodology used to extract rheological observables is detailed.

2.1 Physical problem and modelling assumptions

Geometry and boundary conditions

The simulated flow corresponds to a classical plane Couette configuration, illustrated in figure 2.1. The granular material is confined between two parallel rigid walls separated by a distance h. The upper wall moves with velocity $+U$ while the lower wall moves with velocity $-U$, generating a shear flow within the granular assembly.

The mean shear rate imposed at the walls is

$$\dot{\gamma} = \frac{2U}{h}. \tag{2.1}$$

In a dense granular assembly the actual velocity profile may deviate from strict linearity due to heterogeneous deformation and shear banding. Equation 2.1 therefore defines the kinematic boundary condition imposed at the walls, not an assumption on the bulk behaviour.

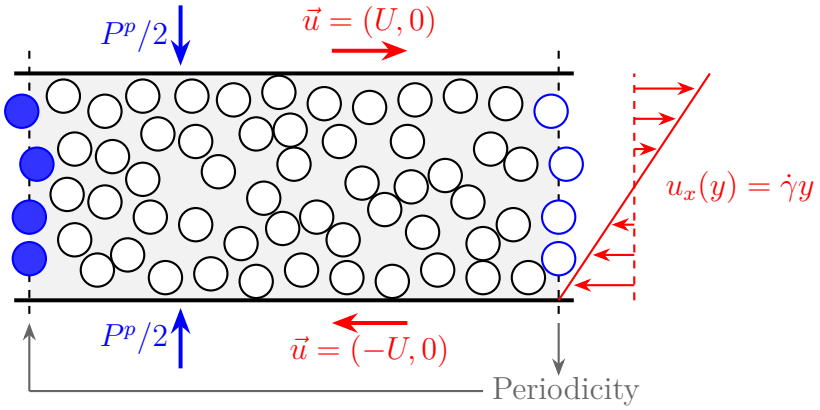

Figure 2.1: Plane Couette configuration used in the simulations. The granular assembly (white particles) is confined between two rigid walls moving at $\pm U$, imposing a mean shear rate $\dot{\gamma}$, and a uniform particle pressure $P^p/2$ is applied normally to both walls. Ghost particles (blue) enforce streamwise periodicity.

Periodic boundary conditions are imposed along the flow direction to reproduce an infinitely extended system and eliminate finite-size effects. A constant normal stress (confinement pressure P^p) is applied in the vertical direction, allowing the domain height h to evolve dynamically until the assembly reaches a packing fraction consistent with the imposed stress state. Rheological quantities are extracted by time-averaging once a steady regime has been identified.

Modelling assumptions

In order to make the problem tractable while preserving the essential physical mechanisms governing dense granular flows, the following modelling assumptions are introduced [22]:

- Dry granular medium: no interstitial fluid is considered. The rheology is entirely controlled by contact interactions between grains, as discussed in section 1.4.

- Cohesionless particles: attractive forces such as capillary, van der Waals, or electrostatic effects are neglected.
- Rigid grains: particles are assumed rigid; only small numerical overlaps arise as a contact regularisation artefact in the soft-sphere limit, but are kept negligible.
- Frictional contact law: interactions are governed by a Coulomb friction model at each contact.
- Dense regime: the flow remains in a dense state, dominated by enduring contacts and force chains rather than dilute binary collisions ($I \lesssim 10^{-1}$, see section 1.3).
- Negligible gravity: gravitational effects are neglected to isolate shear-driven and confinement-driven phenomena.
- Two-dimensional geometry: particles are modelled as circular disks confined within a planar domain (see below), reducing computational cost while retaining the essential physics of dense granular flows.

Dimensional reduction

In principle, the physical problem is three-dimensional and composed of spherical particles. However, the configuration considered in this work is restricted to two dimensions, in which particles are modelled as circular disks confined within a planar domain, as illustrated in figure 2.2. This two-dimensional approach retains the essential physical mechanisms of dense granular flows, including particle rearrangements, force chain formation, and shear-induced dilation, while significantly reducing computational cost.

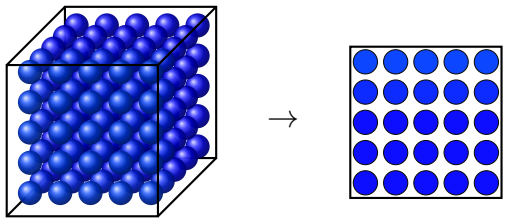

Figure 2.2: Dimensional reduction from the three-dimensional physical system (left) to the two-dimensional representation used in the simulations (right), in which spheres are replaced by circular discs confined within a planar domain.

2.2 Discrete Element Method

As motivated in section 1.4, the Discrete Element Method is the simulation approach of choice for dry dense granular flows. Rather than treating the granular assembly as an effective continuum, DEM resolves the motion of each individual particle and computes contact forces explicitly, providing direct access to the microscopic quantities that govern macroscopic rheology.

The DEM was originally introduced by Cundall and Strack [10] in the context of geomechanics. Since then, it has become the standard numerical tool for granular simulations. Two main families of DEM exist, distinguished by their treatment of contacts:

- In soft-sphere DEM [10], particles are allowed to overlap slightly, and contact forces are computed from penalty-based spring-dashpot models as a function of the overlap between two bodies. This formulation is physically intuitive and easy to implement, but requires very small time steps to resolve the spring oscillation, which becomes computationally costly for stiff particles.
- In hard-sphere (non-smooth) DEM, particles are treated as truly rigid: no overlap is permitted and contacts are resolved as instantaneous impulse-based constraints. This removes the need for small time step, allowing much larger steps while rigorously enforcing non-penetration. The price is a more complex contact resolution algorithm.

In this work, the Non-Smooth Contact Dynamics (NSCD) method [27, 28, 29] is adopted, which belongs to the hard-sphere family and is described in detail below.

In the NSCD framework, the equations of motion of the particles are formulated in terms of impulses rather than instantaneous forces. Over a time step Δt, the velocity update for particle i reads:

$$m_i \left(\mathbf{v}_i^{n+1} - \mathbf{v}_i^n\right) = \sum_{c \in \mathcal{C}_i} \mathbf{p}_i^c,$$

and analogously for rotation. All three contact constraints are enforced simultaneously at the impulse level:

- Signorini's condition: impenetrability and no attractive normal force.
- Newton's restitution law : inelastic impacts.
- Coulomb's friction law: tangential impulse bounded by $\mu\, r_n$, where r_n is the normal impulse.

This implicit formulation allows large time steps and constitutes the principal advantage of NSCD over soft-sphere DEM.

The system of contact impulses is solved iteratively using the Non-Linear Gauss-Seidel (NLGS) algorithm: contacts are visited in sequence, and at each contact the impulse is updated locally to satisfy all three contact conditions while holding the other impulses fixed. This step is repeated until the change in relative velocity at each contact falls below a prescribed tolerance ξ. Convergence is monitored contact by contact via a queue-based strategy that concentrates computational effort on unconverged contacts.

To prevent particles from travelling more than a fraction of their radius per sub-step, the time step Δt is subdivided into n_{sub} sub-steps:

$$n_{\text{sub}} = \max\left(n_{\min},\ \left\lceil \frac{8\, v_{\max}\, \Delta t}{r_{\min}} \right\rceil\right),$$

where $v_{\max}$ is the maximum particle speed and $r_{\min}$ the minimum particle radius. If NLGS convergence is not achieved within a sub-step, the sub-step is recursively halved with an corresponding adapted tolerance, up to a maximum of $n_{\max} = 5$ splits; beyond this the simulation advances regardless to prevent indefinite stalling.

Once the impulses are determined, velocities are updated by adding $\mathbf{p}^c/m_i$ to $\mathbf{v}_i^n$, and positions are advanced by a first-order implicit (backward Euler) scheme:

$$\mathbf{x}_i^{n+1} = \mathbf{x}_i^n + \mathbf{v}_i^{n+1}\, \frac{\Delta t}{n_{\text{sub}}}.$$

2.3 Implementation in *MigFlow*

The DEM described in the previous section is implemented within *MigFlow*[1] [12], an open-source numerical framework developed jointly by UCLouvain and the University of Montpellier for the simulation of immersed granular and multiphase flows. In its general form, *MigFlow* couples the NSCD-based DEM for the granular phase with a stabilised finite-element solver for the fluid phase, following the two-phase averaging framework of Anderson and Jackson [25, 26] described in section 1.4.2. The two solvers are treated as independent modules, so that the fluid can be deactivated entirely without modifying the granular solver.

In the present work, as justified in section 1.4, only the granular component is active. The fluid phase and the fluid-grain coupling are therefore entirely inactive. The grain dynamics are govern by the equations of motion where all forces on

[1] Model for Immersed Granular Flows

the particles arise exclusively from contact interactions resolved by the NLGS algorithm.

System initialisation

The computational domain is created and the initial particle configuration generated inside it. To obtain a stable and homogeneous initial state, particles are arranged on a hexagonal (triangular lattice) packing, illustrated in figure 2.3 and constructed from the two basis vectors

$$\mathbf{a}_1 = (d,\, 0), \qquad \mathbf{a}_2 = \left(\frac{d}{2},\, \frac{\sqrt{3}}{2}d\right),$$

where $d = 2r$ is the particle diameter. Particle centres are placed at $\mathbf{x}_{i,j} = i\,\mathbf{a}_1 + j\,\mathbf{a}_2$, with integers i, j chosen so that all particles remain inside the domain. In this configuration, each particle has six equidistant neighbours, corresponding to the densest possible packing of identical discs in two dimensions, with maximum packing fraction

$$\phi_{\max,2D} = \frac{\pi}{2\sqrt{3}} \approx 0.907,$$

obtained by dividing the area occupied by particles in the reference cell ($3 \times \pi r^2/6$) by the total cell area ($d \times \frac{\sqrt{3}}{2}d$), as illustrated in figure 2.3. This value significantly exceeds the three-dimensional random close-packing fraction $\phi_{rcp,3D} \approx 0.64$ and even the 3D crystalline maximum $\phi_{\max,3D} \approx 0.7405$ [16]. Particles in the bulk are initialised with the affine velocity profile $v_x = \dot{\gamma}\, y$ to reduce the transient period before the steady state is reached.

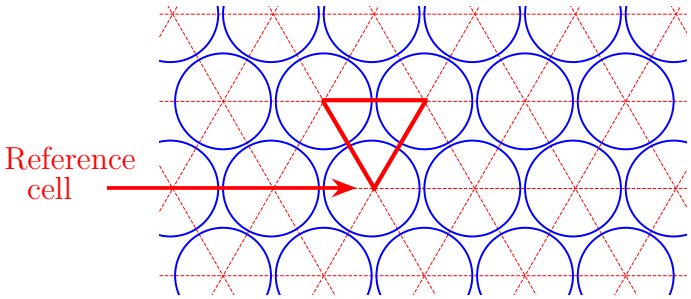

Figure 2.3: Initial hexagonal packing of monodisperse particles (blue) in the computational domain. The reference cell [30] is highlighted in red; its area and particle content give $\phi_{\max,2D} = \pi/(2\sqrt{3})$.

Boundary conditions and periodic remapping

The top and bottom walls are modelled as rigid bodies. A constant normal stress P^p is applied in the vertical direction, allowing the domain height h to adapt dynamically. Shear is imposed by prescribing horizontal velocities $v_{\text{wall}} = \pm U$ to each wall. Contact detection and force resolution between wall and particle follow the same NSCD procedure as for particle-particle contacts, using a separate wall-particle friction coefficient μ_{wp} (see simulation parameters below).

Periodicity in the streamwise direction is enforced through ghost particles: whenever a particle crosses a lateral boundary, an identical copy is placed on the opposite side of the domain at the same relative position. Before contact detection at each time step, particles that have crossed a lateral boundary are remapped back into the domain:

$$x_i \leftarrow \left(x_i + \frac{3w}{2}\right) \bmod w \; - \; \frac{w}{2},$$

which shifts the particle by exactly one domain width w, as shown in figure 2.4, while preserving its velocity and all other state variables.

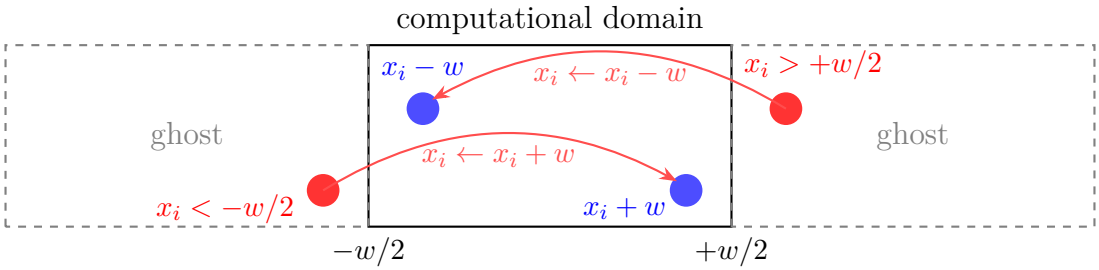

Figure 2.4: Periodic remapping procedure: a particle crossing the right (resp. left) boundary is instantaneously shifted by $-w$ (resp. $+w$) back into the computational domain, preserving all state variables.

Simulation parameters

The reference simulation parameters are summarised in table 2.1. The domain aspect ratio $w/h = 2$ and the ratio of domain height to particle diameter $h/2r = 50$ ensure that the assembly contains a statistically representative number of particles across the confinement direction. The particles are initially arranged on the hexagonal lattice described above, yielding $N = 5103$ particles and an initial packing fraction $\phi_{\text{init}} = N\pi r^2/wh \approx 0.802$.

Table 2.1: Reference simulation parameters.

Parameter	Symbol	Value
Domain height	h	$0.1\,\mathrm{m}$
Domain width	w	$0.2\,\mathrm{m}$
Mean particle radius	r	$1 \times 10^{-3}\,\mathrm{m}$
Particle density	ρ_p	$1000\,\mathrm{kg\,m^{-3}}$
Imposed particle pressure	P^p	$5\,\mathrm{Pa}$
Imposed shear rate	$\dot{\gamma}$	$10\,\mathrm{s^{-1}}$
Wall–particle friction coefficient	μ_{wp}	1.0
Particle–particle friction coefficient	μ_{pp}	0.4
Numerical time step	Δt	$10^{-3}\,\mathrm{s}$
Final simulation time	t_{end}	$10\,\mathrm{s}$

The imposed pressure and shear rate yield an inertial number

$$I = \frac{\dot{\gamma}\, d}{\sqrt{P^p/\rho_p}} = \frac{10 \times 2 \times 10^{-3}}{\sqrt{5/1000}} \approx 0.28,$$

placing the reference simulation in the dense inertial regime ($10^{-3} \leq I \leq 1$). The inter-particle friction coefficient $\mu_{\mathrm{pp}} = 0.4$ is a standard value for dense granular assemblies [22], while the wall friction $\mu_{\mathrm{wp}} = 1.0$ is set higher to prevent wall slip.

Overall algorithm

The overall simulation algorithm is illustrated in figure 2.5. After initialisation, the simulation advances by repeating the following steps at each time step: wall boundary conditions are updated (confinement pressure and imposed shear velocity); periodic remapping is applied; contact detection identifies all active pairs; the NLGS solver iterates to convergence; velocities and positions are updated; and macroscopic quantities are computed and written to output.

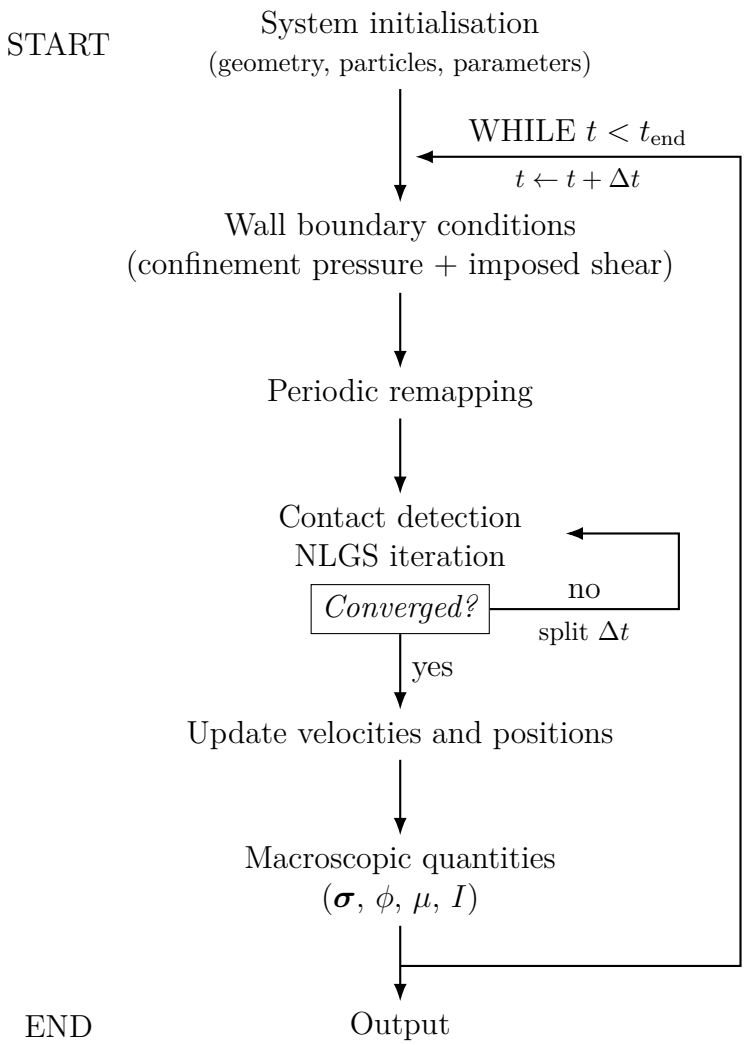

Figure 2.5: Flowchart of the *MigFlow* simulation algorithm. Macroscopic quantities are computed at every time step but averaged only over the steady-state window identified in post-processing (section 2.4).

2.4 Post-processing and macroscopic observables

Macroscopic observables

The following macroscopic quantities are computed from the particle data at each time step.

- Packing fraction: The two-dimensional surface packing fraction is

$$\phi = \frac{\sum_{i=1}^{N} \pi r_i^2}{A},$$

where N is the number of particles, r_i their radius, and $A = w\,h(t)$ the current domain area. For monodisperse particles the maximum achievable value corresponds to the hexagonal close-packing fraction [16, 30]. Considering the reference cell illustrated in figure 2.3, the area occupied by the particles within the cell being $3 \times \pi r^2/6$ and the total area of the reference cell being $r \times \sqrt{3}\,r$.

$$\phi_{\max,2D} = \frac{\pi}{2\sqrt{3}} \approx 0.907,$$

significantly larger than the three-dimensional random close-packing value $\phi_{rcp,3D} \approx 0.64$ and larger than $\phi_{max,3D} \approx 0.7405$ for ordered crystalline packings [16].

- Stress tensor: The averaged stress tensor is computed from the contact forces using the Love-Weber formula [31]:

$$\sigma_{ij} = \frac{1}{A} \sum_{c \in \mathcal{C}} f_i^c \, \ell_j^c,$$

where the sum runs over all particle-particle contacts $\mathcal{C}$, $\mathbf{f}^c$ is the contact force exerted on particle 0 of contact c, $\boldsymbol{\ell}^c = \mathbf{x}_1^c - \mathbf{x}_0^c$ is the branch vector connecting the two particle centres (corrected for periodicity). The three independent components of interest are the normal stresses σ_{xx} and σ_{yy}, and the shear stress τ_{xy}.

- Effective friction coefficient: The effective friction coefficient μ characterises the macroscopic frictional response of the assembly and is defined as the time average of the ratio of the shear stress to the normal stress in the compression direction:

$$\mu = \frac{\left|\langle \tau_{xy} \rangle_t\right|}{\left|\langle \sigma_{yy} \rangle_t\right|}$$

- Inertial number: For a monodisperse system, equation 1.1 describes the inertial number I with $d = 2r$. For polydisperse systems, d is replaced by the mean branch length ℓ_b introduced in section 1.3.1, which constitutes the physically grounded characteristic length scale of the contact network:

$$I = \frac{\dot{\gamma}\,\ell_b}{\sqrt{P^p/\rho_p}}, \qquad \ell_b = \langle |\mathbf{r}_i - \mathbf{r}_j| \rangle_{\text{contacts}}. \tag{2.2}$$

Steady-state detection

The initial phase of any simulation is dominated by transient effects. Upon application of shear, the granular assembly reorganises internally : the contact network reorients to support the shear load, particles undergo non-affine displacements, and the macroscopic observables ϕ, τ, and μ exhibit significant time dependence.

In this work, the domain height h is used as the primary convergence indicator. Under imposed pressure, the walls are free to move and h evolves until the assembly reaches the packing fraction compatible with the imposed stress and shear state. Once h stabilises (i.e. a dynamic equilibrium is reached between energy input through boundary motion and energy dissipation through frictional contacts), the transient regime is considered over, and rheological quantities can be extracted.

A robust and automated procedure combining two complementary criteria has been implemented to identify the steady-state, as illustrated in figure 2.6.

- Oscillation-based criterion

  The final mean height h_{conv} is estimated as the average of the last 100 time steps. The signal $h(t) - h_{\text{conv}}$ is then analysed for zero-crossings. A small numerical tolerance $\varepsilon = 10^{-4} h_{\text{conv}}$ is introduced in order to avoid spurious sign changes near zero. The steady state is considered to be reached after $n_{\text{osc}} = 4$ complete oscillations, corresponding to $2n_{\text{osc}} = 8$ sign changes. The convergence index $t^{(1)}_{\text{conv}}$ is defined as the time corresponding to the eighth crossing. This criterion ensures that the assembly undergoes several successive cycles of compression and dilation before being considered stationary.

- Stabilisation criterion

  A sliding window of 100 consecutive time steps is swept forward in time. For each window position i, the relative deviation $|h(t) - h_{\text{conv}}|/h_{\text{conv}}$ is evaluated for every point within the window. A window is considered stable if at least 95% of its points remain within a tolerance of 0.5%. The convergence index $t^{(2)}_{\text{conv}}$ is then defined as the starting time of the first stable window. This criterion guarantees that the fluctuations are not only bounded, but also statistically stable over a sustained time interval.

The final convergence time t_{conv} is defined as the earliest time satisfying either of the two criteria, while enforcing a lower bound of 10% of the total simulation time. This definition ensures that the system is not considered stationary too early.

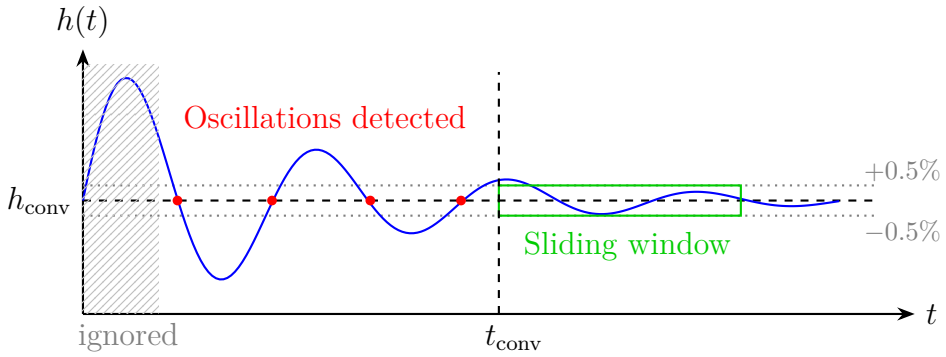

Figure 2.6: Illustration of the two-criterion steady-state detection method. The hatched region corresponds to the transient phase that is ignored. The red dots highlight the oscillations and the green sliding window verifies convergence from t_{conv} onwards.

Once the steady state is identified, macroscopic quantities are computed by averaging over $t \geq t_{\text{conv}}$. For the reference simulation ($t_{\text{end}} = 10\,\text{s}$, $t_{\text{conv}} \approx 3.6\,\text{s}$), this corresponds to approximately 1200 time steps, providing a sufficient statistical sample. The rheological quantities extracted following this averaging procedure are presented and discussed in the following chapter.

Chapter 3

Results

This chapter presents and analyses the results obtained from numerical simulations of plane Couette shear of dense granular assemblies using the *MigFlow* framework. Building on the steady-state detection procedure introduced in the previous chapter, the goal of this chapter is to characterise the jamming transition in monodisperse assemblies and to quantify the effect of polydispersity on the macroscopic rheology.

The chapter is organised as follows. First, the transient dynamics are examined and the steady-state detection procedure is validated on the reference monodisperse simulation. The rheological behaviour is then characterised over a wide range of inertial numbers, and the crystallisation-induced jamming threshold is identified and explained. A systematic comparison between mono- and polydisperse assemblies follows. Finally, the sensitivity of the constitutive parameters of the $\mu(I)$-law to the polydispersity level λ is quantified.

3.1 Toward steady state

Overview of the transient phase

The simulation is initialised from a perfect hexagonal lattice, which represents the densest admissible arrangement of monodisperse discs in two dimensions. Due to the imposed shear rate on the walls, the system will undergo a structural reorganisation before any meaningful rheological measurement can be extracted. The structural evolution is illustrated in figure 3.1, which shows snapshots of the assembly at $t = 0$, 1, 2, 3, 6 and 10 s, while figure 3.2 tracks the four primary macroscopic observables over time: the domain height $h(t)$, the solid fraction $\phi(t)$, the shear stress $\tau(t)$, and the effective friction coefficient $\mu(t)$.

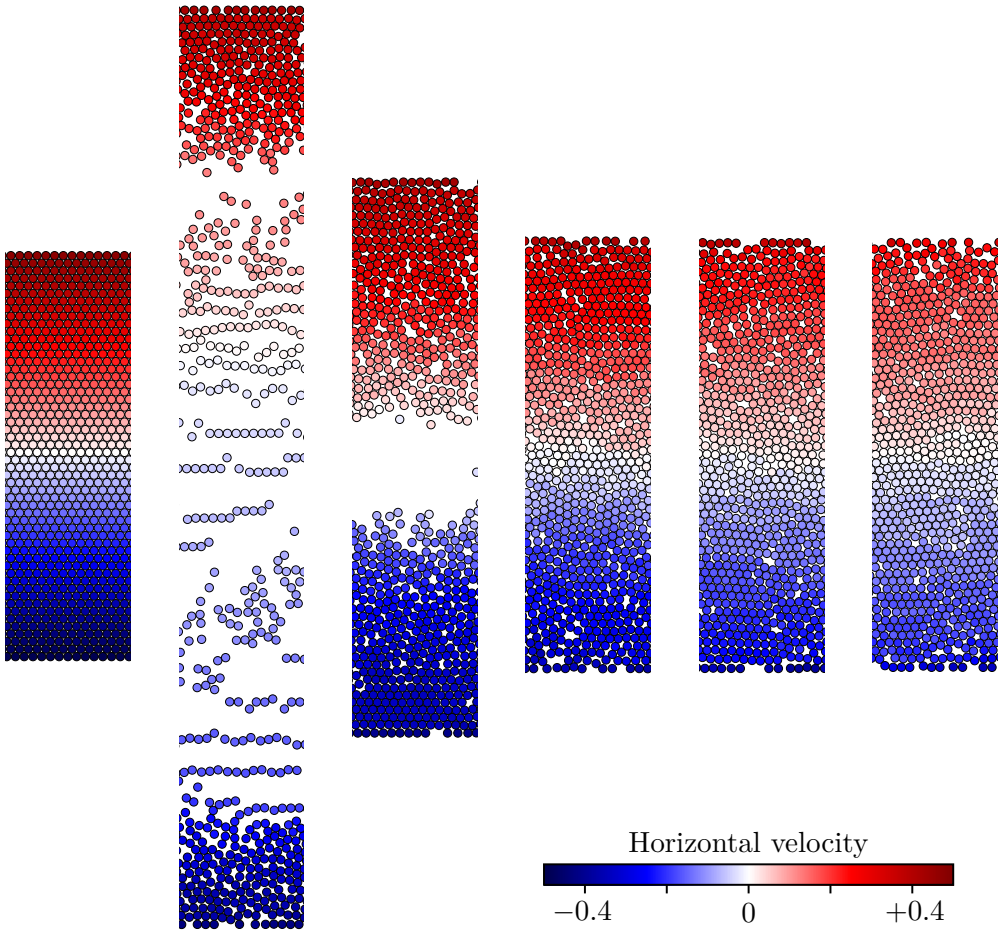

Figure 3.1: Snapshots of the granular assembly at successive times. Colours indicate the instantaneous horizontal velocity of each particle. From left to right: $t = 0$ s (initial ordered hexagonal configuration), $t = 1$ s (disordered state), $t = 2 - 3$ s (recompaction), and $t = 6 - 10$ s (established steady shear flow regime).

The early dynamics are dominated by the Reynolds dilatancy effect [1, 32]: a dense granular assembly cannot shear without first expanding, since neighbouring particles must climb over one another to allow relative sliding, which necessarily increases the total volume. At $t = 0^+$, the suddenly applied shear is far from equilibrium with the internal stress state of the dense lattice. Particles are abruptly dislodged from their crystalline positions, generating a large excess of free volume: the domain height overshoots to $h \approx 0.25$ m at $t \approx 1$ s, while the solid fraction drops from $\phi_{\text{init}} \approx 0.802$ to a minimum of $\phi \approx 0.35$, a value closer to a dilute

granular gas than of a dense assembly [33]. This near-fluidisation phase is visible in the snapshot at $t = 1$ s (figure 3.1), where particles are scattered throughout the domain.

The kinetic energy injected during this initial disruption is progressively dissipated through two mechanisms [2, 5, 28]: inelastic collisions, which reduce the kinetic energy of each binary impact, and frictional sliding at grain contacts, which converts mechanical energy into heat irreversibly . As dissipation proceeds, the imposed confinement pressure drives a recompaction: the walls converge, ϕ rises back toward its equilibrium value, and the domain height undergoes damped oscillations. These oscillations reflect the competition between the elastic restoring effect of the contact network and the inertia of the granular assembly [1], and their attenuation marks the approach to the steady state.

The steady-state detection algorithm described in the previous chapter identifies $t_{\mathrm{conv}} \approx 3.6$ s as the onset of stationarity, at which point h stabilises at $h_{\mathrm{conv}} \approx 0.104$ m and $\phi \approx 0.767$. This value lies well below the hexagonal close-packing limit $\phi_{\max} \approx 0.907$ and also below the random close-packing fraction $\phi_{\mathrm{rcp}} \approx 0.82$-$0.84$ reported for two-dimensional monodisperse disc assemblies [16]. This confirms that the shear-driven steady state is intrinsically disordered and less compact than either the initial crystal or the densest disordered packing.

The shear stress $\tau(t)$ provides a complementary picture of the transient. A sharp negative spike of amplitude $|\tau| \approx 30$ Pa appears at $t \approx 2$ s, coinciding with the minimum of $h(t)$ during recompaction. This stress overshoot is a signature of the dilatancy cycle in dense granular flows [1] as the assembly recompacts under the applied pressure. Beyond this singular event, τ settles to a stationary mean $\langle\tau\rangle \approx 1.89$ Pa with standard deviation $\sigma_\tau \approx 0.42$ Pa. The relative fluctuation level $\sigma_\tau/|\langle\tau\rangle| \approx 22\%$ is consistent with the strong heterogeneity of stress transmission expected in the dense inertial regime.[17].

Among all observables, the effective friction coefficient $\mu(t)$ exhibits the most pronounced fluctuations. During the transient, μ exhibits large excursions over [0, 0.8], reflecting the rapid succession of contact creation and destruction. These fluctuations are physically associated with the intermittent collapse and reformation of force-chain networks [2, 17, 34]. As the system approaches steady state, μ oscillates around $\langle\mu\rangle \approx 0.392$. This value is in good agreement with the two-dimensional discrete simulations of da Cruz et al. [22], who reported the same ranges for μ for frictional discs in the dense inertial regime.

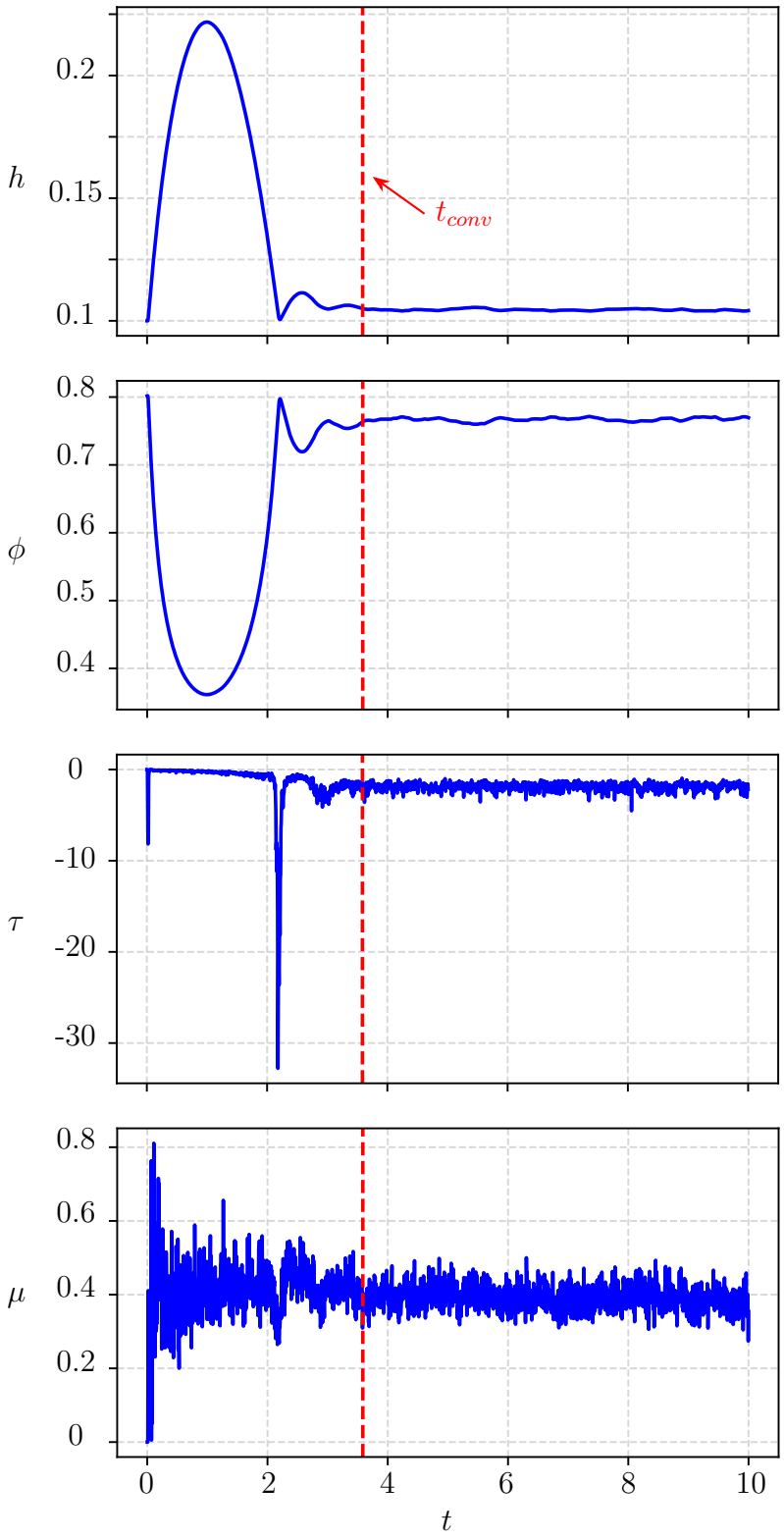

Figure 3.2: From top to bottom, temporal evolution of the system height h, solid fraction ϕ, shear stress τ, and effective friction coefficient μ.

Established steady state

A critical check on the correctness of the simulation is provided by the time-averaged normal stress component σ_{yy}, which represents the mechanical pressure exerted by the granular assembly on the confining walls. In steady state:

$$\langle \sigma_{yy} \rangle = 4.81\text{Pa},$$

in excellent agreement with the imposed particle pressure $P^p = 5$ Pa (relative error $\approx 3.8\%$). This close match confirms that the pressure-controlled boundary conditions are correctly enforced throughout the simulation. The residual discrepancy is attributable to (i) the finite size of the time-averaging window, and (ii) the intrinsic fluctuations of the discrete contact dynamics, which prevent exact point-wise satisfaction of the pressure balance at every instant.

Table 3.1: Steady-state macroscopic quantities for the reference monodisperse simulation ($P^p = 5$ Pa, $\dot{\gamma} = 10$ s^{-1}).

Quantity	Symbol	Value
Convergence height	h_{conv}	0.104 m
Solid fraction	$\langle \phi \rangle$	0.767 ± 0.003
Effective friction	$\langle \mu \rangle$	0.392 ± 0.033
Shear stress	$\langle \tau \rangle$	-1.89 ± 0.42 Pa
Normal stress x-dir.	$\langle \sigma_{xx} \rangle$	4.53 ± 0.92 Pa
Normal stress y-dir.	$\langle \sigma_{yy} \rangle$	4.81 ± 1.03 Pa
Number of contacts	N_c	15045
Inertial number	I	0.283

All steady-state macroscopic quantities for the reference simulation are summarised in table 3.1. An important observation is the stress anisotropy $\sigma_{xx} \neq \sigma_{yy}$: the horizontal normal stress (4.53 Pa) is systematically lower than the vertical one (4.81 Pa). This anisotropy is a direct signature of the shear-induced reorganisation of the contact network: under shear, force chains preferentially align at an angle to the flow direction [22], which concentrates normal forces in the compression direction (here y) relative to the flow direction (x). The first normal stress difference $N_1 = \sigma_{xx} - \sigma_{yy}$ is thus negative, consistent with experimental observations in dense granular flows [24].

Figure 3.3 shows the instantaneous horizontal velocity u_x sampled along a vertical column at $x = 0$ and $t = 10$ s, i.e. well within the established steady-state regime. For each height y, the velocity of the particle whose cross-section contains the point $(0, y)$ is recorded and regions between particles appear as $u_x = 0$. The profile increases monotonically from $u_x \approx -U$ near the lower wall to $u_x \approx +U$ near the

upper wall, with no significant disturbance. This linear trend confirms that the bulk shear rate is spatially uniform and close to the wall-imposed value $\dot{\gamma} = 10\ \mathrm{s}^{-1}$, justifying the use of equation 2.1 to characterise the flow state.

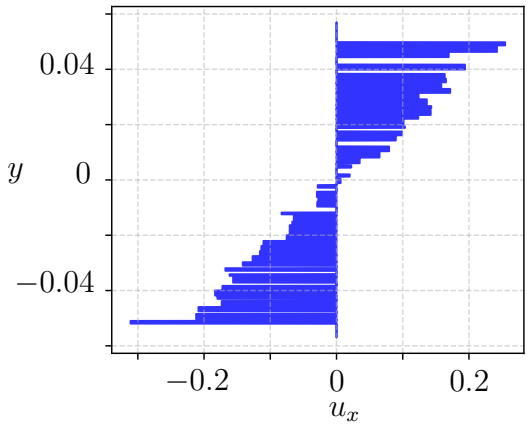

Figure 3.3: Instantaneous horizontal velocity u_x sampled along the vertical column $x = 0$ at $t = 10$ s (reference monodisperse simulation, $\dot{\gamma} = 10\ \mathrm{s}^{-1}$, $P^p = 5$ Pa). Each filled region corresponds to the velocity of the particle whose cross-section covers that height; gaps between particles appear as $u_x = 0$. The monotonically increasing profile confirms spatially uniform shear.

3.2 Rheological behaviour and jamming

Probing the $\mu(I)$ and $\phi(I)$ relations

Having characterised the reference simulation at $\dot{\gamma} = 10\ \mathrm{s}^{-1}$, the rheological behaviour is now explored over a wider range of inertial numbers. The shear rate is varied systematically from $0.1\ \mathrm{s}^{-1}$ to $20\ \mathrm{s}^{-1}$ while keeping $P^p = 5$ Pa fixed, nominally covering $I \in [3 \cdot 10^{-3}, 6 \cdot 10^{-1}]$.

Figure 3.4 presents the resulting values of μ and ϕ as functions of I. Two qualitatively different outcomes are observed:

- Flowing states ($I \gtrsim 0.20$, filled markers): the assembly reaches a statistically stationary regime. The results confirm the expected trends of the $\mu(I)$ framework [11, 22]: μ increases with I (from 0.392 at $I \approx 0.28$ to 0.525 at $I \approx 0.57$), while ϕ decreases (from 0.767 to 0.706), consistent with the dense inertial flow regime.
- Jammed states ($I \lesssim 0.20$, open markers): the assembly never reaches a flowing steady state. Instead, it spontaneously orders into a periodic hexagonal lattice

and ceases to flow. These points cannot be used to infer a constitutive law, as the system is no longer in a flowing state.

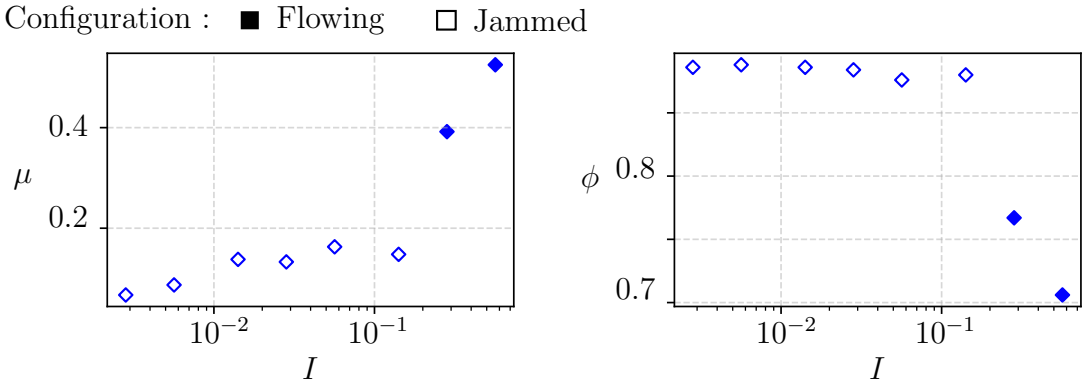

Figure 3.4: Effective friction coefficient μ (left) and solid fraction ϕ (right) as functions of I for the monodisperse system. Filled markers: steady flowing states. Open markers: simulations in which the assembly crystallised and jammed.

Physical mechanism of crystallisation-induced jamming

The behaviour observed between flowing and jammed configurations in figure 3.5 reflects a known feature of two-dimensional monodisperse systems: since all particles are identical, they can, under suitable conditions, spontaneously organise into a dense hexagonal crystalline packing. Once such a crystal spans the periodic domain, the contact network stiffens and collective rearrangements are suppressed. The assembly of grains no longer flows but the crystalline block is not strictly immobile: it undergoes slow, rigid-body-like drift as a whole.

In the present simulations, this transition is governed by the inertial number I. At high I, the shear rate is fast enough to continuously disrupt any emerging order, and the system remains in a disordered flowing state. At low I, the deformation is slow relative to particle rearrangement ($\tau_\gamma = 1/\dot{\gamma} \gg \tau_r = d/\sqrt{P^p/\rho_p}$), leaving sufficient time for the assembly to rearrange toward the hexagonal configuration before the next shear-induced displacement. Because all particles are identical and the geometry is periodic, this ordered state is fully compatible with the boundary conditions. Figure 3.5 illustrates this contrast at $t = 10$ s for $\dot{\gamma} = 10$ s^{-1} ($I \approx 0.28$, disordered flow) and $\dot{\gamma} = 5$ s^{-1} ($I \approx 0.14$, crystallised arrest).

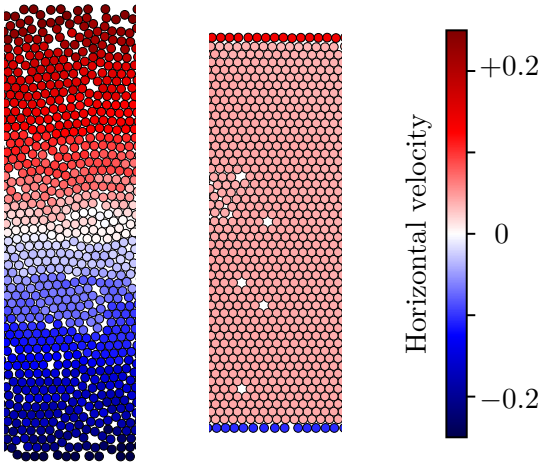

Figure 3.5: Particle configurations at $t = 10$ s for two shear rates: $\dot{\gamma} = 10\,s^{-1}$ ($I \approx 0.28$, left, flowing disordered state) and $\dot{\gamma} = 5\,s^{-1}$ ($I \approx 0.14$, right, crystallised jammed state). Particles are colour-coded by instantaneous horizontal velocity u_x.

Consequences and transition to polydisperse systems

In this present configuration, the crystallisation threshold is bracketed between $\dot{\gamma} = 5$ s^{-1} (jammed, $I \approx 0.14$) and $\dot{\gamma} = 10$ s^{-1} (flowing, $I \approx 0.28$), giving $I_c \in [0.14, 0.28]$. Below I_c, the system crystallises before reaching a rheological steady state, which prevents probing the $\mu(I)$ and $\phi(I)$ curves at lower inertial numbers.

To explore what happens at lower inertial numbers under the same present configuration, polydispersity is introduced. The idea is to frustrate long-range periodic ordering and suppress crystallisation in sheared granular systems by introducing a modest spread in particle sizes. Whether jamming can still occur in this setting and how the $\mu(I)$ and $\phi(I)$ curves extend toward the quasi-static regime, is the subject of the following section.

3.3 Comparative analysis: monodisperse vs. polydisperse systems

Setup and characterisation of polydispersity

To investigate the effect of particle size distribution on the macroscopic rheology, a polydisperse assembly is constructed with a uniform radii distribution in $[r_{\min}, r_{\max}]$ $= [0.8, 1.2]$ mm, yielding a polydispersity level $\lambda = d_{\max}/d_{\min} = 1.5$. The mean

diameter $\bar{d} \approx 2$ mm is kept identical to the monodisperse reference, ensuring that any observed differences are attributable to the size distribution rather than a change in scale. As established in section 1.3.1, the relevant length scale for computing the inertial number in polydisperse systems is the mean branch length ℓ_b. For the polydisperse system under reference conditions, $\ell_b = 2.03$ mm, slightly larger than the monodisperse value $\ell_b^{\text{mono}} = 2.00$ mm, reflecting the wider geometric variability of the contact network introduced by the size distribution.

Steady-state macroscopic quantities

The introduction of a moderate polydispersity level ($\lambda = 1.5$) modifies the macroscopic response of the system, as summarised in table 3.2 for both systems at $P^p = 5$ Pa and $\dot{\gamma} = 10$ s^{-1}.

Table 3.2: Steady-state macroscopic quantities for the monodisperse and polydisperse ($\lambda = 1.5$) systems at $P^p = 5$ Pa, $\dot{\gamma} = 10$ s^{-1}.

Quantity	Monodisperse	Polydisperse ($\lambda = 1.5$)
h_{conv} (m)	0.1043	0.1100
$\langle\phi\rangle$	0.767 ± 0.003	0.736 ± 0.002
$\langle\mu\rangle$	0.392 ± 0.033	0.469 ± 0.043
$\langle\tau\rangle$ (Pa)	-1.89 ± 0.42	-2.22 ± 0.43
$\langle\sigma_{xx}\rangle$ (Pa)	4.53 ± 0.92	4.78 ± 1.10
$\langle\sigma_{yy}\rangle$ (Pa)	4.81 ± 1.03	4.74 ± 0.92
Number of contacts N_c	15045	15986
Mean branch length ℓ_b (mm)	2.00	2.03
Inertial number	0.28	0.29

The solid fraction decreases from 0.767 to 0.736 (about 4 %), while the number of contacts increases slightly from 15 045 to 15 986 (roughly 6 %). These two observations are seemingly contradictory but can be in fact two facets of the same mechanism. In the monodisperse case, identical particles can sometimes arrange into locally ordered structures, achieving a locally efficient packing. With mild polydispersity ($\lambda = 1.5$), the size contrast is too small for smaller particles to fill interstitial voids between larger ones, yet large enough to frustrate the formation of such ordered regions. The assembly is therefore geometrically less efficient, resulting in a lower solid fraction. At the same time, the absence of any lattice structure and the spatial heterogeneity of the contact network, visible in figure 3.6, means that particles are more randomly positioned relative to their neighbours, increasing the likelihood of surface contacts throughout the assembly and thus raising N_c despite the looser packing.

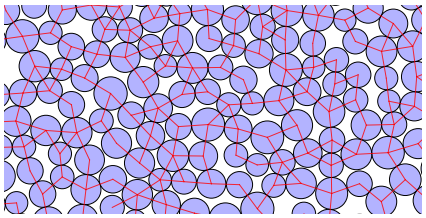

Figure 3.6: Instantaneous contact network for the polydisperse system ($\lambda = 1.5$) at $t = 10$ s. Branch vectors (red lines) connect the centres of contacting particles.

The imposed pressure condition is satisfied within 6 % in both cases ($\langle\sigma_{yy}\rangle \approx P^p = 5$Pa), confirming the robustness of the numerical framework across different particle size distributions. Regarding the effective friction coefficient, it increases from 0.392 to 0.469 (about 20 %), and the mean shear stress rises in magnitude from 1.89 Pa to 2.22 Pa (about 17 %). Although the size distribution does not fundamentally alter the global flow dynamics, it introduces sufficient geometric disorder to measurably increase both the frictional resistance and the shear stress of the assembly.

This result is in partial agreement with [35], who showed that shear strength is largely independent of polydispersity in dense granular flows for inertial numbers $I \in [2 \times 10^{-4}, 0.1]$. However, the present simulations operate at $I \approx 0.28$, which lies outside that range, in the inertial regime where particle rearrangements are more frequent and the contact network is more transient. It is therefore not surprising that polydispersity has a non-negligible effect on the macroscopic rheology at this higher inertial number.

Rheological behaviour: $\mu(I)$ and $\phi(I)$ relations

Figure 3.7 presents the $\mu(I)$ and $\phi(I)$ curves obtained by varying $\dot{\gamma}$ for both systems. They both follow the expected qualitative trends of the $\mu(I)$ framework: μ increases with I while ϕ decreases. However, for the studied inertial numbers the polydisperse system exhibits a higher μ and a lower ϕ than its monodisperse counterpart. This offset appears as a near-rigid vertical shift of both curves, suggesting that polydispersity at this level rescales the rheological response without altering its functional form. The $\mu(I)$ framework is therefore applied to the polydisperse system and the different coefficients of this law extracted.

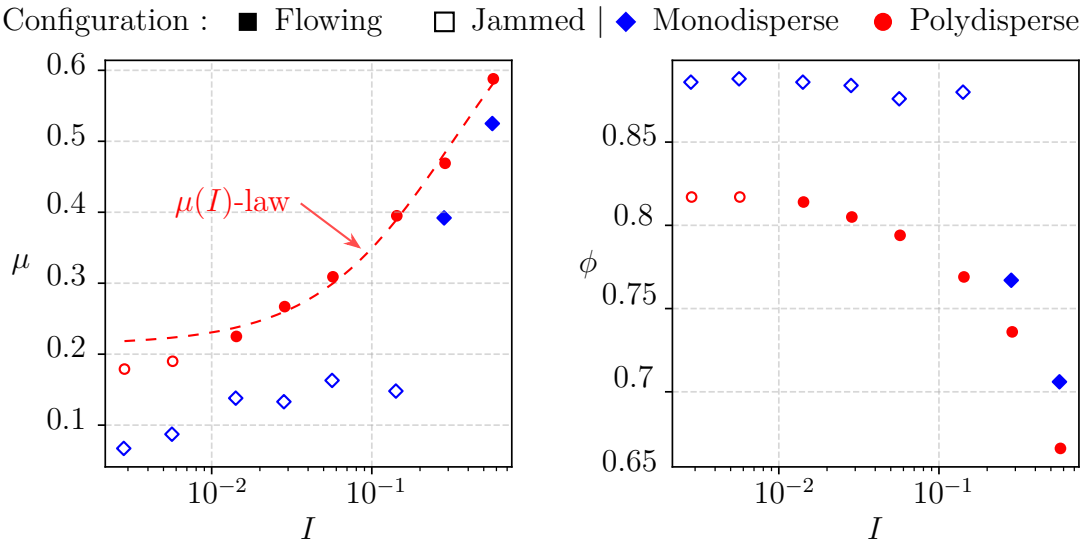

Figure 3.7: Effective friction coefficient μ (left) and packing fraction ϕ (right) as functions of the inertial number I (logarithmic scale), for the monodisperse (blue) and polydisperse (red) systems. The red dashed line corresponds to the $\mu(I)$ law fit. The inertial number is varied by changing the shear rate $\dot{\gamma}$.

Using the nonlinear least squares (Trust Region Reflective algorithm), the $\mu(I)$-law was fitted on the polydisperse flowing data and the corresponding coefficients were extracted :

$$\mu_s = 0.21, \qquad \mu_2 = 0.79, \qquad I_0 = 0.32.$$

These values are broadly consistent with those reported by [22] for two-dimensional assemblies of frictional discs ($\mu_s = 0.25$), although a direct comparison is limited by the fact that da Cruz et al. employ a linearised friction law, from which I_0 cannot be extracted independently. A comparison with the three-dimensional results of Jop et al. [11] ($\mu_s \approx 0.38$, $\mu_2 \approx 0.64$, for glass beads on a rough inclined plane) is not straightforward given the dimensional difference. The somewhat lower μ_s obtained here is nonetheless qualitatively expected in two dimensions, where the contact geometry and the number of force-chain directions are more restricted than in three dimensions.

Suppression of crystallisation by polydispersity

A key practical advantage of polydisperse assemblies is the suppression of crystallisation and, consequently, of crystallisation-induced jamming. As shown in figure 3.7 (logarithmic scale), the monodisperse data terminate at $I \approx 0.2$, below which no steady flowing state can be obtained. The polydisperse data, in contrast,

extend down to $I \approx 10^{-2}$, closer to the quasi-static regime. The physical reason is straightforward: the geometric disorder introduced by the particle size distribution permanently frustrates the formation of any periodic crystalline arrangement, so the contact network remains disordered at all inertial numbers.

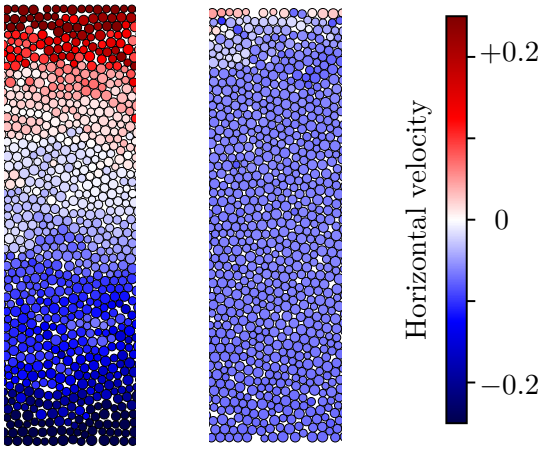

Figure 3.8: Polydisperse particle configurations at $t = 10$ s for two shear rates: $\dot{\gamma} = 1\,s^{-1}$ ($I \approx 0.029$, left, flowing disordered state) and $\dot{\gamma} = 0.1\,s^{-1}$ ($I \approx 0.0029$, right, jammed state). Particles are colour-coded by instantaneous horizontal velocity u_x.

However, jamming is not entirely eliminated in polydisperse systems: at sufficiently low inertial numbers, a disordered arrest is observed, distinct in nature from the crystalline jamming of the monodisperse case. Rather than locking into a periodic lattice, the assembly freezes into an amorphous configuration in which the disordered contact network becomes rigid and no further rearrangements can occur. Figure 3.8 illustrates this contrast clearly: in the flowing state, a velocity gradient is observed across the height of the system, whereas in the jammed state the velocity field becomes spatially uniform, indicating there is no relative particle motion and the assembly is kinematically blocked. This suggests that while polydispersity removes the geometric instability toward crystallisation, it does not suppress the more general jamming transition associated with the divergence of the contact network rigidity as $I \to 0$. Probing this limit systematically is left for future work.

3.4 Effect of polydispersity level

To go beyond the reference case $\lambda = 1.5$ and assess how the magnitude of size dispersity affects the rheology and the jamming transition, simulations are performed

for a range of polydispersity levels: $\lambda \in \{1.22, 1.5, 2.33, 9\}$.

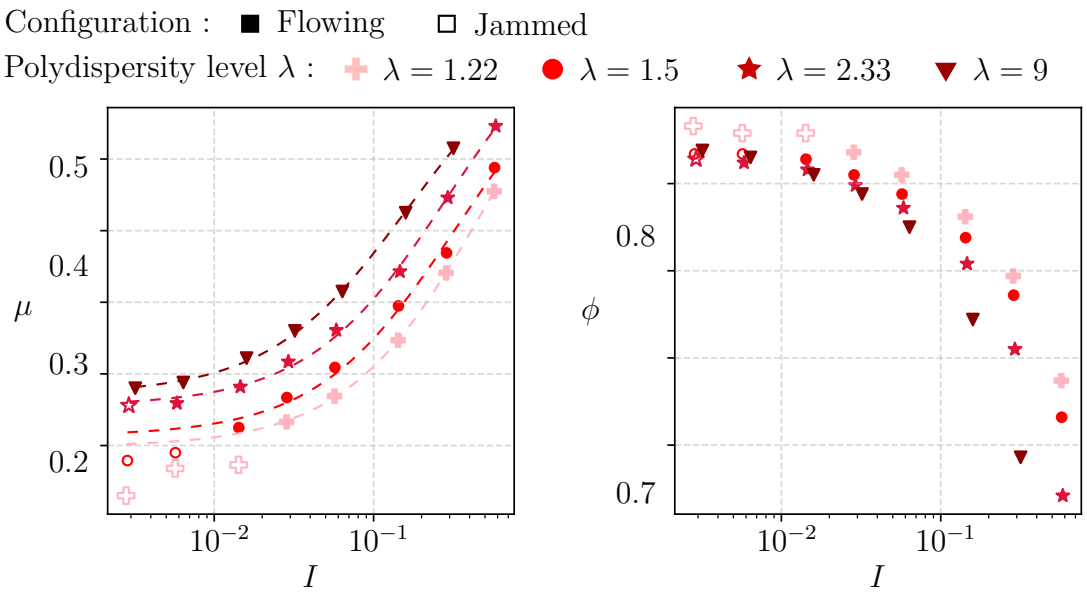

Figure 3.9: Effective friction coefficient μ (left) and packing fraction ϕ (right) as functions of the inertial number I, for four polydispersity levels ($\lambda \in 1.22, 1.5, 2.33, 9$), all with uniform distribution and mean particle diameter $\overline{d} \approx 2\,mm$.

Figure 3.9 presents the $\mu(I)$ and $\phi(I)$ curves for all values of λ. Several systematic trends emerge. The effective friction coefficient μ increases monotonically with λ at every inertial number. This is attributed to the growing contact density: in a more polydisperse assembly, small particles fill the interstitial voids between larger ones, generating additional grain–grain contacts and hence more frictional dissipation pathways than in a nearly monodisperse system (where the maximum coordination number is bounded by the hexagonal geometry). The packing fraction ϕ, conversely, decreases monotonically with λ. As the size ratio broadens, the geometric frustration of optimal packing intensifies: no single arrangement allows all particles to settle simultaneously into their most compact local configuration, so the steady-state density is progressively reduced. Both trends are fully consistent with the physical picture established for $\lambda = 1.5$ and confirm that polydispersity acts as a systematic tuning parameter for both μ and ϕ.

The fitted parameters of the $\mu(I)$-law for each polydispersity level are collected in table 3.3. The quasi-static friction coefficient μ_s increases steadily from 0.198 at $\lambda = 1.22$ to 0.272 at $\lambda = 9$, reflecting the growing frictional resistance as the contact network becomes denser. The inertial limit μ_2 remains approximately constant around 0.82 ± 0.04, suggesting that at large inertial numbers the collisional

contribution to stress is relatively insensitive to the size distribution. The transition scale I_0 decreases monotonically from 0.493 to 0.163 as λ increases, indicating that the crossover from quasi-static to inertial behaviour occurs at progressively lower inertial numbers.

Table 3.3: Fitted parameters of the $\mu(I)$-law (equation 1.2) for each polydispersity level λ. The fit is performed by nonlinear least squares on the flowing data only.

λ	μ_s	μ_2	I_0
1.22	0.198	0.862	0.493
1.50	0.213	0.790	0.324
2.33	0.255	0.836	0.289
9.00	0.272	0.790	0.163

3.5 Discussion

The $\mu(I)$ rheology, originally established for monodisperse granular systems, extends naturally to polydisperse assemblies. Polania [35] demonstrated numerically that all samples, regardless of their polydispersity level, collapse onto the constitutive friction law proposed by Jop et al. [11]. More specifically, for inertial numbers $I \lesssim 0.1$, the effective friction coefficient μ is essentially independent of the polydispersity level, at least for $\lambda \in [1.2, 8.0]$. This result, first established in the quasi-static regime, extends to the dense flow regime and confirms that the $\mu(I)$ rheology remains a valid descriptor for polydisperse granular flows.

The results presented in this work, stand in contrast with the findings of Polania. In the present simulations, a monotonic increase of μ with λ is observed across the entire range of inertial numbers explored, including at $I \approx 10^{-2}$. The difference in dimensionality may explain this discrepancy: Polania's simulations are three-dimensional, whereas the present work is strictly two-dimensional. This might constrain the contact network, which amplifies the sensitivity of μ to the size distribution. Clarifying this point, notably through a 3D extension of the present simulations, would be a priority for future work.

Conclusion

This thesis has investigated the multi-scale rheology of dense dry granular assemblies under plane Couette shear, through systematic numerical simulations performed with the MigFlow framework. The main findings can be summarised as follows.

Monodisperse assemblies were first simulated across a range of inertial numbers. The expected trends of the $\mu(I)$ rheology were recovered in the flowing regime: the effective friction coefficient μ increases and the packing fraction ϕ decreases with I. However, below a critical threshold $I_c \in [0.14, 0.28]$, identical particles spontaneously organise into a hexagonal crystalline lattice, causing jamming and preventing any exploration of the quasi-static regime.

Introducing polydispersity (uniform radius distribution, $\lambda = d_{max}/d_{min}$ up to 9) effectively suppresses crystallisation by permanently frustrating long-range periodic ordering, allowing steady flowing states to be reached down to $I \approx 10^{-3}$. The $\mu(I)$ rheological framework remains valid across all polydispersity levels tested: μ increases and ϕ decreases monotonically with I, but in contrast with Polania's three-dimensional findings, the constitutive parameters of the $\mu(I)$-law were found to evolve systematically with λ. Finally, it was observed that a disordered jamming transition persists at very low inertial numbers even in polydisperse systems, distinct in nature from the crystalline arrest of the monodisperse case.

Taken together, these results confirm that the MigFlow framework correctly reproduces the $\mu(I)$ rheology for dry granular assemblies, and provide a systematic quantification of how polydispersity shifts the constitutive parameters of this law.

Several directions for future work emerge naturally from this study. On the numerical side, extending the simulations to three dimensions would allow direct comparison with existing 3D experimental and numerical datasets, and would test whether the crystallisation-jamming mechanism and the polydispersity effects identified here survive in a higher-dimensional setting. On the physical side, reintroducing the interstitial fluid phase, for which the *MigFlow* framework is already equipped, would allow the full immersed granular flow problem to be addressed, bridging the dry granular limit studied here with the viscous suspension framework.

Bibliography

[1] B. Andreotti, Y. Forterre, and O. Pouliquen, *Granular Media: Between Fluid and Solid*. Cambridge: Cambridge University Press, 2013.

[2] H. M. Jaeger, S. R. Nagel, and R. P. Behringer, "Granular solids, liquids, and gases," *Reviews of Modern Physics*, vol. 68, pp. 1259–1273, Oct. 1996.

[3] H. M. Jaeger, T. Shinbrot, and P. B. Umbanhowar, "Does the granular matter?," *Proceedings of the National Academy of Sciences of the United States of America*, vol. 97, pp. 12959–12960, Nov. 2000.

[4] A. Mehta, *Granular Physics*. Cambridge: Cambridge University Press, 2007.

[5] GDR MiDi, "On dense granular flows," *The European Physical Journal E*, vol. 14, pp. 341–365, Aug. 2004.

[6] H. P. Zhu, Z. Y. Zhou, R. Y. Yang, and A. B. Yu, "Discrete particle simulation of particulate systems: Theoretical developments," *Chemical Engineering Science*, vol. 62, pp. 3378–3396, July 2007.

[7] E. C. P. Breard, L. Fullard, and J. Dufek, "Rheology of granular mixtures with varying size, density, particle friction, and flow geometry," *Physical Review Fluids*, vol. 9, p. 054303, May 2024.

[8] M. Kamali Zarch, L. Zhang, S. M. Haeri, and J. He, "Classic, modern, and physics-based rheological laws for geophysical granular flows in a landslide hazard chain," *Earth-Science Reviews*, vol. 269, p. 105204, Oct. 2025.

[9] O. Polanía, M. Renouf, M. Cabrera, N. Estrada, and E. Azéma, "Monodisperse behavior of polydisperse flows," *Physical Review E*, vol. 111, p. L043401, Apr. 2025.

[10] P. A. Cundall and O. D. L. Strack, "A discrete numerical model for granular assemblies," *Géotechnique*, vol. 29, pp. 47–65, Mar. 1979.

[11] P. Jop, Y. Forterre, and O. Pouliquen, "A constitutive law for dense granular flows," *Nature*, vol. 441, pp. 727–730, June 2006.

[12] M. Constant, F. Dubois, J. Lambrechts, and V. Legat, "Implementation of an unresolved stabilised FEM–DEM model to solve immersed granular flows," *Computational Particle Mechanics*, vol. 6, pp. 213–226, Apr. 2019.

[13] W. B. Russel, D. A. Saville, and W. R. Schowalter, *Colloidal Dispersions*. Cambridge Monographs on Mechanics, Cambridge: Cambridge University Press, 1989.

[14] A. J. Liu and S. R. Nagel, "Jamming is not just cool any more," *Nature*, vol. 396, pp. 21–22, Nov. 1998.

[15] D. Bi, J. Zhang, B. Chakraborty, and R. P. Behringer, "Jamming by shear," *Nature*, vol. 480, pp. 355–358, Dec. 2011.

[16] S. Torquato and F. H. Stillinger, "Jammed hard-particle packings: From Kepler to Bernal and beyond," *Reviews of Modern Physics*, vol. 82, pp. 2633–2672, Sept. 2010.

[17] F. Radjai, D. E. Wolf, S. Roux, M. Jean, and J. J. Moreau, "Force networks in dense granular media," May 1997.

[18] H. A. Barnes, *An introduction to rheology*. Rheology series ; 3, Amsterdam: Elsevier, 4th impr. ed., 1996.

[19] R. Hooke, *Lectures de potentia restitutiva, or of spring*. 1678.

[20] S. I. Newton, *Philosophiae naturalis principia mathematica*. 1687.

[21] J. D. Ferry, *Viscoelastic Properties of Polymers*. John Wiley & Sons, Sept. 1980. Google-Books-ID: 9dqQY3Ujsx4C.

[22] F. da Cruz, S. Emam, M. Prochnow, J.-N. Roux, and F. Chevoir, "Rheophysics of dense granular materials: Discrete simulation of plane shear flows," *Physical Review E*, vol. 72, p. 021309, Aug. 2005.

[23] O. Pouliquen and Y. Forterre, "A non-local rheology for dense granular flows," *Philosophical Transactions: Mathematical, Physical and Engineering Sciences*, vol. 367, no. 1909, pp. 5091–5107, 2009.

[24] Guazzelli and O. Pouliquen, "Rheology of dense granular suspensions," *Journal of Fluid Mechanics*, vol. 852, Oct. 2018.

[25] R. Jackson, "Locally averaged equations of motion for a mixture of identical spherical particles and a Newtonian fluid," *Chemical Engineering Science*, vol. 52, pp. 2457–2469, Aug. 1997.

[26] T. B. Anderson and R. Jackson, "Fluid Mechanical Description of Fluidized Beds. Stability of State of Uniform Fluidization," *Industrial & Engineering Chemistry Fundamentals*, vol. 7, pp. 12–21, Feb. 1968.

[27] M. Jean, "The non-smooth contact dynamics method," *Computer Methods in Applied Mechanics and Engineering*, vol. 177, pp. 235–257, July 1999.

[28] J. J. Moreau, "Some numerical methods in multibody dynamics: application to granular materials," *European Journal of Mechanics - A/Solids*, vol. 13, no. 4 Suppl., pp. 93–114, 1994.

[29] M. Henry, *Numerical methods for granular media in multiphase fluids*. PhD thesis, UCL - Université Catholique de Louvain, Sept. 2025.

[30] L. Fukshansky, "Revisiting the hexagonal lattice: on optimal lattice circle packing," *Elemente der Mathematik*, vol. 66, pp. 1–9, Jan. 2011.

[31] F. Nicot, N. Hadda, M. Guessasma, J. Fortin, and O. Millet, "On the definition of the stress tensor in granular media," *International Journal of Solids and Structures*, vol. 50, pp. 2508–2517, July 2013.

[32] O. Reynolds, "LVII. On the dilatancy of media composed of rigid particles in contact. With experimental illustrations," *Philosophical Magazine*, vol. 20, pp. 469–481, Dec. 1885.

[33] N. V. Brilliantov and T. Pöschel, *Kinetic Theory of Granular Gases*. Oxford University Press, July 2004.

[34] T. S. Majmudar and R. P. Behringer, "Contact force measurements and stress-induced anisotropy in granular materials," *Nature*, vol. 435, pp. 1079–1082, June 2005.

[35] O. Polania, *Polydispersity in Granular Flows : Exploring Effects in Dry and Submerged Environments*. Theses, Université de Montpellier ; Universidad de los Andes (Bogotá, Colombia ; 1948-....), Dec. 2023. Issue: 2023UMONS061.

UNIVERSITÉ CATHOLIQUE DE LOUVAIN
École polytechnique de Louvain
Rue Archimède, 1 bte L6.11.01, 1348 Louvain-la-Neuve, Belgique | **www.uclouvain.be/epl**